Article

Neuron

Combinatorial Targeting of Distributed Forebrain Networks Reverses Noise Hypersensitivity in a Model of Autism Spectrum Disorder

Highlights

- ASD model (Ptchd1 KO) shows deficits in automatic and goal-directed noise filtering
- Automatic filtering is explained by sensory thalamic deficits
- Goal-directed filtering is explained by prefrontal deficits
- Combinatorial targeting of both deficits rescued noise hypersensitivity

Authors

Miho Nakajima, L. Ian Schmitt, Guoping Feng, Michael M. Halassa

Correspondence

mhalassa@mit.edu

In Brief

"Sensory overload" is common in autism spectrum disorder (ASD). By identifying multiple circuit abnormalities underlying perturbed automatic and goal-directed filtering in one ASD model, Nakajima et al. develop a combinatorial treatment strategy that fully normalizes noise hypersensitivity in that model.

Nakajima et al., 2019, Neuron *104*, 488–500
November 6, 2019
https://doi.org/10.1016/j.neuron.2019.09.040

CellPress

CellPress

Neuron
Article

Combinatorial Targeting of Distributed Forebrain Networks Reverses Noise Hypersensitivity in a Model of Autism Spectrum Disorder

Miho Nakajima,[1,3] L. Ian Schmitt,[1,3] Guoping Feng,[1,2] and Michael M. Halassa[1,2,4,*]
[1]McGovern Institute for Brain Research and the Department of Brain and Cognitive Science, Massachusetts Institute of Technology, Cambridge, MA, USA
[2]The Stanley Center for Psychiatric Genetics, Broad Institute of Harvard and MIT, Cambridge, MA, USA
[3]These authors contributed equally
[4]Lead Contact
*Correspondence: mhalassa@mit.edu
https://doi.org/10.1016/j.neuron.2019.09.040

SUMMARY

Autism spectrum disorder (ASD) is associated with noise hypersensitivity, the suboptimal extraction of meaningful signals in noisy environments. Because sensory filtering can involve distinct automatic and executive circuit mechanisms, however, developing circuit-specific therapeutic strategies for ASD noise hypersensitivity can be challenging. Here, we find that both of these processes are individually perturbed in one monogenic form of ASD, *Ptchd1* deletion. Although Ptchd1 is preferentially expressed in the thalamic reticular nucleus during development, pharmacological rescue of thalamic perturbations in knockout (KO) mice only normalized automatic sensory filtering. By discovering a separate prefrontal perturbation in these animals and adopting a combinatorial pharmacological approach that also rescued its associated goal-directed noise filtering deficit, we achieved full normalization of noise hypersensitivity in this model. Overall, our work highlights the importance of identifying large-scale functional circuit architectures and utilizing them as access points for behavioral disease correction.

INTRODUCTION

Aberrant sensory processing is one of the best recognized features of autism spectrum disorder (ASD). Patients often describe difficulties "filtering" sensory inputs, and "sensory overload" is frequently encountered in clinical practice (Marco et al., 2011; Tomchek and Dunn, 2007). Despite this, little is known about the precise nature of sensory processing deficits in ASD: their neurobiology and their contribution to attentional and cognitive abnormalities. Gaining mechanistic insight would thus provide currently unknown points of entry for disease modification to impact attention and overall cognitive function in this disorder.

In previous work, we identified a circuit abnormality in a mouse model of ASD, the PTCHD1 knockout (KO) (Wells et al., 2016). PTCHD1 is a sonic hedgehog receptor family protein whose deletion in humans is associated with 1% of all ASD with intellectual disability (Chaudhry et al., 2015; Filges et al., 2011; Marshall et al., 2008; Noor et al., 2010; Pinto et al., 2010). During development, *Ptchd1* is selectively enriched in the thalamic reticular nucleus (TRN), a shell of GABAergic neurons surrounding the thalamus that provides its major inhibitory input (Halassa and Acsády, 2016; Pinault, 2004). Our work identified a reduction in small conductance, Ca^{2+}-activated potassium channel (SK) activity (Cueni et al., 2008) within TRN neurons of this model. Pharmacological correction of this deficit in a broad behavioral screen rescued attentional deficits and hyperactivity, but not memory deficits, aggression, and hypotonia (Wells et al., 2016).

Although the ability to rescue certain sensory processing deficits by targeting the TRN is of therapeutic potential, the involvement of multiple brain systems in the KO model raises the possibility that it may be insufficient for clinically relevant behavioral correction. Specifically, although the TRN is a key node for automatic sensory filtering, providing inhibition to refine and filter sensory inputs, TRN activity is under "top-down" control of the prefrontal cortex (PFC) (Nakajima et al., 2019). As such, in a disease state such as that modeled by the KO, it is unclear whether deficits in sensory filtering can be fully explained by TRN abnormalities or also involve failures in its top-down control. This is likely to be even more true in the majority of ASD cases arising from polygenic risk factors that almost certainly impact multiple brain systems (Intaitė et al., 2019).

In this study, we adopted a circuit-level approach investigating the nature of noise hypersensitivity in the KO. We focused on auditory-guided behavior, as it allowed us to parametrically adjust noise and signal characteristics. Consistent with prior studies (Wells et al., 2016), we found some abnormalities in auditory processing that are explained by TRN dysfunction. However, we also identified deficits in top-down control of TRN function that were attributed to suboptimal encoding and maintenance of task-relevant information in the PFC. Based on these insights, we devised a combinatorial treatment targeting both prefrontal and thalamic circuits. This treatment fully rescued noise hypersensitivity and restored PFC-dependent

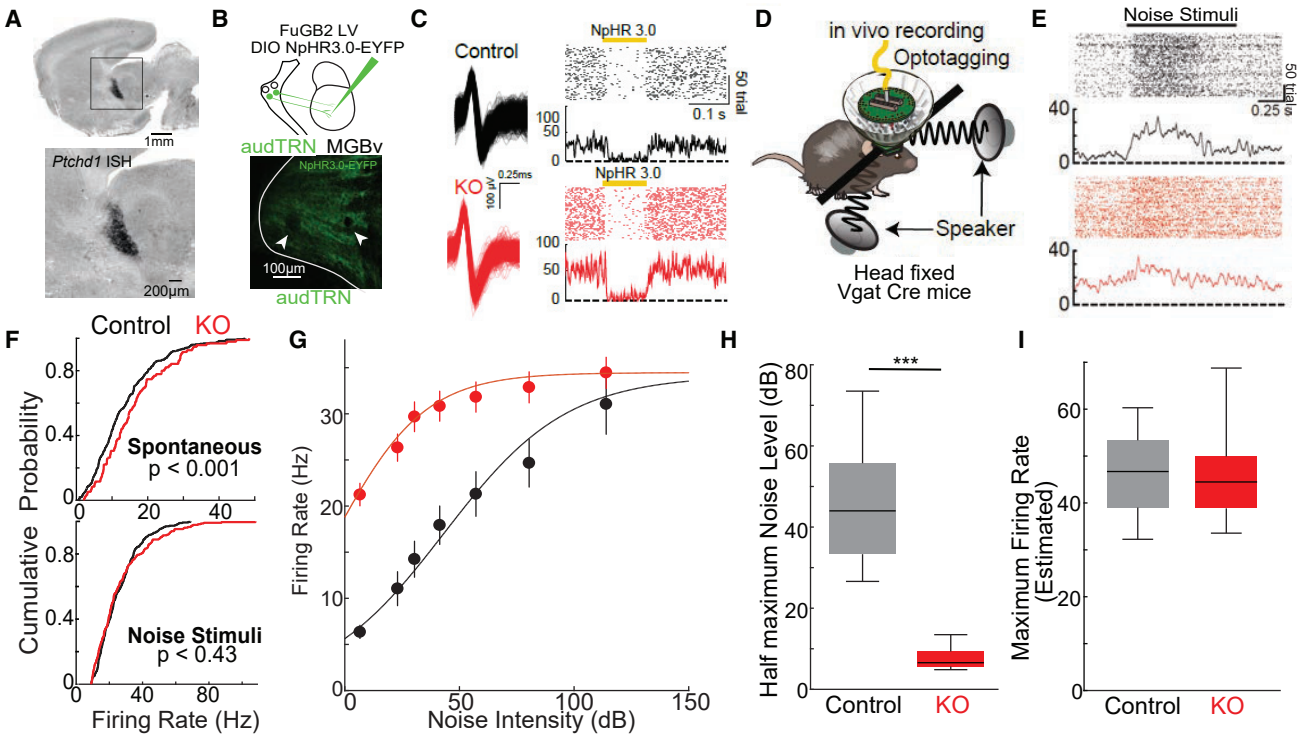

Figure 1. Sound-Evoked Responses of audTRN Neurons Are Diminished in the KO

(A) *In situ* hybridization showing expression of *PtchD1* in TRN during early development (P0).

(B) Top: strategy to label audTRN neurons. MGBv-projecting audTRN neurons were selectively labeled by injecting the MGBv of Vgat Cre mice with retrograde lentivirus (FuGB2LV) harboring Cre-dependent NpHR3.0-EYFP. Bottom: example confocal image shows electrode tips lesions and NpHR3.0-EYFP expression in the audTRN.

(C) Left: example audTRN waveforms in control (top, black) and KO (bottom, red) mice. Right: peri-stimulus time histograms (PSTHs) and rasters show short latency optogenetic suppression (100 ms, yellow bar) of audTRN neurons via NpHR3.0 in control (black) or KO (red) mice.

(D) Schematic of head-fixed recording with multi-electrode drive targeting audTRN to record sound responses. Sound was presented binaurally by two speakers.

(E) Example PSTHs and rasters showing diminished sound responses (1 s, black bar) of audTRN neurons in KO (bottom) compared to control (top).

(F) Cumulative probability plot of audTRN firing rates before (spontaneous, top) or during the sound presentation (noise stimuli, bottom) recorded across control (black, N = 3 mice, 602 neurons) and KO (red, N = 3 mice, 468 neurons) animals (Kolmogorov-Smirnov test).

(G) Average firing rate of control (black) and KO (red) audTRN neurons in response to increasing intensity noise stimuli. KO audTRN neurons showed high firing at lower noise level but smaller increase across intensities (N = 3 control; 3 KO mice; n = 88 control; 447 KO neurons; error bars show SEM).

(H) Estimated noise level required to reach the inflection point (corresponding to the half maximum of the sigmoidal fit) based on control and KO neuron responses in (G). Half-maximal values were significantly lower in KO compared with controls ($p < 0.001$; rank-sum test).

(I) Estimated maximum firing rates of control and KO neurons. Estimates did not significantly differ between groups ($p = 0.06$; rank-sum test).

Boxplots: median (line); quartiles (box); 95% confidence interval (whiskers). See also Figure S1.

control over sensory filtering in the KO. Collectively, these results highlight the benefits of targeting treatments for neurodevelopmental disorders based on a distributed circuit level understanding of behavioral functions.

RESULTS

Sensory Responses of Auditory TRN Neurons Are Diminished in PTCHD1 KO Mice

Our previous work had shown that the ASD-linked gene, *Ptchd1*, is selectively expressed in the TRN at birth (Figure 1A) and by postnatal day 15 (P15), expression is widespread across multiple brain regions, including the PFC (Wells et al., 2016). We had also observed that, although KO mice were able to detect the location of visual flashes on par with wild-type littermates, their task performance was sharply impaired when targets were preceded with spatially incongruent visual distractors (Wells et al., 2016). Although these findings are consistent with sensory-related distractibility, the lack of parametric stimulus control in that task made it difficult to precisely link its behavioral results to the more general problem of noise hypersensitivity and map it onto the relevant circuits.

To address these issues, we examined the impact of PTCHD1 deletion on auditory thalamic processing and broadband noise filtering in auditory-guided behavior. We chose to focus on the auditory system for two reasons: first, human ASD patients frequently show hypersensitivity to sounds (Baum et al., 2015; Dunn et al., 2006; Liss et al., 2006; Wiggins et al., 2009) and,

second, characterizing sensory processing deficits in the auditory system is facilitated by the ease of generating and administering auditory stimuli to behaving rodents (Hromádka and Zador, 2009; Juavinett et al., 2018).

Using our previously established methods for tagging TRN subnetworks *in vivo* (Halassa et al., 2014; Nakajima et al., 2019; Wimmer et al., 2015), we targeted the auditory subnetwork projecting to the ventral division of the medial geniculate body (MGBv), which we refer to as the auditory TRN (audTRN). Briefly, we employed an intersectional strategy based on connectivity and genetic identity to optogenetically tag this TRN subnetwork (Figure 1B). Using multielectrode arrays, we evaluated the responses of these identified neurons in head-fixed mice (Figures 1C and 1D). Because these neurons show preferential responses to broadband stimuli (Cotillon-Williams et al., 2008; I. Schmitt et al., 2016, COSYNE, conference; Vaingankar et al., 2012), we delivered mid-intensity broadband auditory noise (Gaussian white noise, 57 dB; see STAR Methods) to both KO and wild-type controls.

Inspection of single-neuron recordings revealed a striking difference between the two groups; although KO audTRN neurons showed significantly higher baseline spike rates compared to control neurons, their firing rate in response to broadband noise was comparable (Figures 1E and 1F). One explanation for these observations is that audTRN neurons in the KO are close to saturation in the absence of sensory input, impeding their ability to increase their firing rate. To test this idea, we measured audTRN responses to increasing levels of broadband noise. We found that the range of their response profile was indeed diminished, with a significantly lower stimulation required to drive half-maximal response (Figures 1G and 1H) but a comparable maximal spike rate (Figure 1I).

To determine whether changes in audTRN neural spiking observed in the KO could be explained by altered intrinsic properties, we performed whole-cell recordings of retrobead-identified audTRN neurons in acute slices (Figure S1A; see STAR Methods). Consistent with previous recordings of TRN neurons not identified based on connectivity (Wells et al., 2016), we found reduced repetitive bursting in KO audTRN neurons (Figures S1B–S1D). Previous data indicated that this bursting phenotype involved diminished SK channel conductance (Wells et al., 2016). Given that SK channels have also been shown to determine neural input/output functions (Deister et al., 2009), we wondered whether their diminished conductance could explain enhanced spontaneous spike rates observed in KO audTRN neurons. As such, we measured the input/output function of audTRN neurons in the slice following step current injections (Luque et al., 2017) and found that KO neurons showed a leftward shift (Figures S1E–S1G). Fitting of response curves to these observations indicated that audTRN spiking in the KO would saturate at a much lower level of current injection compared with control (Figure S1H) but that maximum firing rates would be similar (control: 56 ± 4.9 Hz; KO: 59 ± 2.9 Hz). To approximate dynamically varying sensory input, we employed a 2-step current injection protocol (Figure S1I). Compared to control neurons, responses to additional current were diminished in audTRN KO neurons despite there being no significant change in absolute firing rates on the second current step (Figures S1J and S1K). These findings support a model in which reduced sensory-driven responses in the KO occur because audTRN neurons are already close to their response maximum in the absence of sensory input.

KO Mice Display Neural and Behavioral Hypersensitivity to Auditory Noise

Given that TRN neurons have been reported to engage in feedforward and feedback inhibition of sensory thalamic circuits (Crabtree, 1999, 2018; Cruikshank et al., 2010), we asked whether the KO's diminished audTRN sensory responses impacted auditory processing at the level of MGBv (Hackett et al., 2011; Tsukano et al., 2017).

Recordings of MGBv auditory responses (to appropriately selected stimuli; dynamic random cords [DRCs]; see STAR Methods) revealed that KO MGBv neurons had comparable spontaneous spiking rates to controls (Figures 2A–2C) but that auditory responses of KO MGBv neurons were significantly elevated (Figures 2B and 2C). Critically, KO responses were further elevated and showed degraded temporal precision when noise was added to the stimuli (Figures 2D–2F and S2A). In contrast, control MGBv neurons showed sparser responses and intact temporal precision with similar average firing rate with moderate levels of broadband noise. These results suggest that audTRN dysfunction in the KO produces a hypersensitivity to noise in MGBv neuronal responses.

The impact on MGBv-evoked responses in the KO with relative sparing of spontaneous activity suggested that audTRN preferentially influences MGBv-evoked responses. To investigate this idea, we approximated MGBv responses using a simple linear-non-linear model with two steps: linear input integration and non-linear spike generation (Ostojic and Brunel, 2011; Overath et al., 2015). We generated two variants of the model, in which audTRN suppression impacted either the linear step (corresponding to dendritic inhibition) or the non-linear one (corresponding to peri-somatic inhibition) (Jadi et al., 2012; Miles et al., 1996). The models made different predictions on how audTRN activity suppression would affect MGBv spontaneous versus evoked spike rates (Figures S2B and S2C). To determine which model accurately captured real audTRN/MGBv interactions, we analyzed MGBv spiking data in recordings with optogenetic audTRN suppression (Figure S2D). We found that this manipulation increased evoked MGBv responses without altering spontaneous activity (Figure S2E), supporting a model in which audTRN controls MGBv sensory-input gain (Figures S2B and S2C, model 1). This is consistent with anatomical studies showing that audTRN neurons preferentially innervate MGBv dendrites (Wang et al., 2001) and may explain the selective impact of the KO on evoked, but not spontaneous, MGBv activity.

To examine the consequences of neural noise hypersensitivity in the KO for behavior, we employed a recently developed task (Nakajima et al., 2019) that provides a parametric behavioral readout of noise sensitivity by requiring animals to discriminate auditory signals while the level of background noise levels is varied (Figure 2G). On each trial, a mouse was presented with one of the three different tones (20 kHz, 16 kHz, or 24 kHz; 100-ms duration each). Mice were trained to nose-poke following

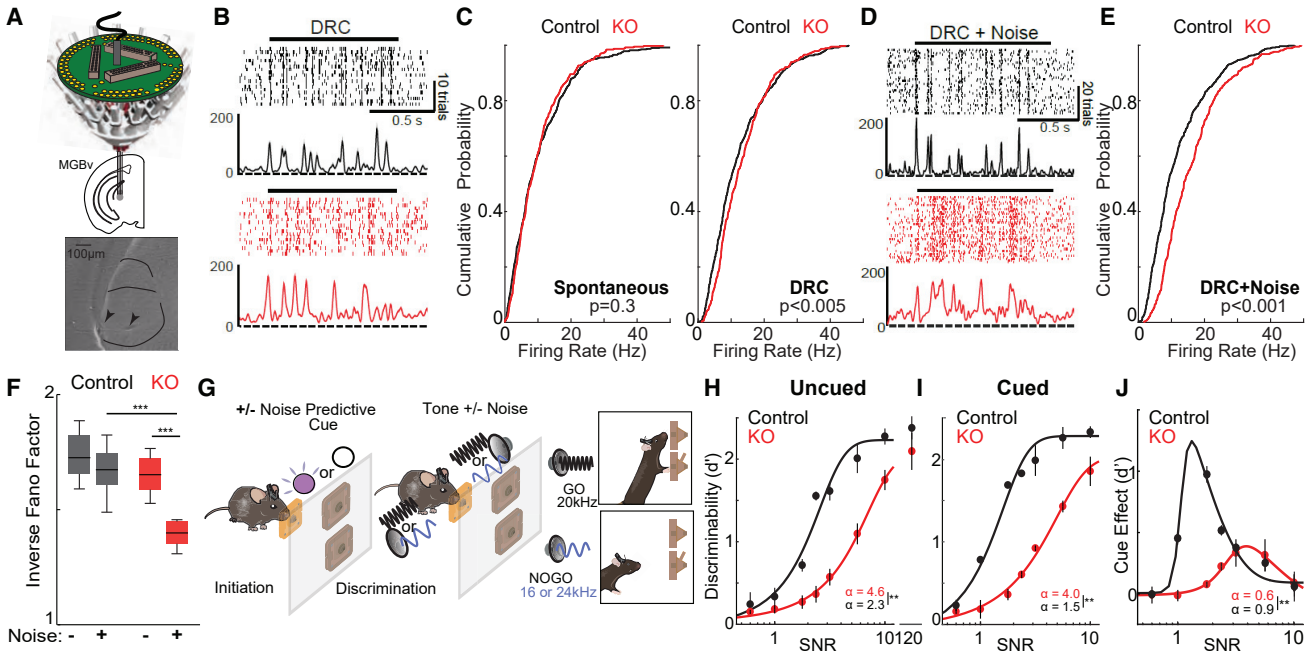

Figure 2. KO Mice Show Noise Hypersensitivity to Sound

(A) Top: schematic of multi-electrode drive targeting the MGBv. Bottom: example brain section shows electrolytic MGBv electrode tip lesions.

(B) Example rasters and PSTHs for a control (black, top) and a KO (red, bottom) MGBv neuron showing responses to a single DRC across trials.

(C) Cumulative probability plots of spontaneous (left) or stimulus (DRC, right) MGBv responses in control (black, N = 3 mice, 424 neurons) and KO (red, N = 3 mice, 235 neurons; Kolmogorov-Smirnov test).

(D) Responses of MGBv neurons in (B) to the same DRC stimulus with broadband noise added (SNR 3.2).

(E) Cumulative probability plot showing MGBv responses to DRCs with broadband noise added (SNR 3.2) in control (black, N = 3 mice, 424 neurons) and KO (red, N = 3 mice, 235 neurons; Kolmogorov-Smirnov test).

(F) Inverse Fano factor values estimated across repeated presentations of dynamic random chords without or with background noise (SNR 3.2). Response consistency was significantly lower in KO (red) under noisy conditions compared to both non-noise conditions and to the noise condition in controls (gray; $p < 6.6 \times 10^{-28}$ multivariate ANOVA [MANOVA] main effect of genotype; N = 3 control, 4 KO mice; n = 211 control, 261 KO neurons; ***p < 0.001; rank-sum test).

(G) Schematic of a cued noisy auditory discrimination (Go/NoGo) task with varying SNR and cueing of "noise" trials (SNR $\leq$ 10). On an interleaved subset of trials, mice were cued with a 100-ms pulse of UV light followed by a 400-ms delay period before target stimulus presentation. After the delay, one of three different tones with varying SNRs was presented for 100 ms (20 kHz for target "Go" tone or 16 and 24 kHz for non-target "NoGo" tones). Following the Go tone, the mouse performed a nose poke in the response port to open a reward port (hit). Following either of the NoGo tones, the mouse was required to withhold until the reward port opens (correct rejection).

(H) Psychometric curve of the performance of KO (red) and control (black) mice on uncued trials. Discrimination threshold and lapse rate were significantly increased compared to control (N = 6 mice per genotype; >14 sessions per condition; **p < 0.01; rank-sum test).

(I) Psychometric curve of the performance of KO (red) and control (black) mice on cued trials. Discrimination threshold and lapse rate were significantly increased compared with control (N = 6 mice; >14 sessions per condition; **p < 0.01; rank-sum test).

(J) Cue effect across SNR levels showing a lower performance improvement in KO (red) compared to control (black) mice (**p < 0.01; rank-sum test).

Boxplots: median (line); quartiles (box); 95% confidence interval (whiskers). Error bars show SEM. See also Figure S2.

presentation of a 20-kHz tone but to withhold following presentation of either 16-kHz or 24-kHz tones. Both appropriate response types (hits and correct rejections) were rewarded (Figure 2G). The signal-to-noise ratio (SNR) of the targets was varied by adding different intensities of broadband background noise. In addition to assessing auditory signal discrimination as a function of background noise, this task provided the ability to engage the executive component of noise filtering by including a noise-predictive cue on some trials (Nakajima et al., 2019). We reasoned that this latter property of the task would allow us to distinguish deficits in automatic noise filtering (uncued trials) from executive controlled noise filtering (cued trials).

Using this approach, we found that, when target stimulus SNR was high (i.e., no background noise was added), KO performance was comparable to controls (Figure 2H; SNR = 120). However, KO performance rapidly degraded if background noise was increased (Figure 2H), as expected based on their neural noise hypersensitivity (Figures 2F and S2A). Intriguingly, although control animals showed significant improvement in performance on a subset of low SNR trials if the noise-predicting cue was presented, enhancement was minimal in the KO (Figures 2I and 2J). These findings suggested that KO mice were unable to use cues to anticipate (and suppress) upcoming noise. Given their behavioral deficit on uncued trials, however, it was difficult to determine whether a deficit in automatic noise filtering potentially attributable to the audTRN was sufficient to explain deficits on cued trials or whether it might involve dysfunction in executive control. As such, we designed

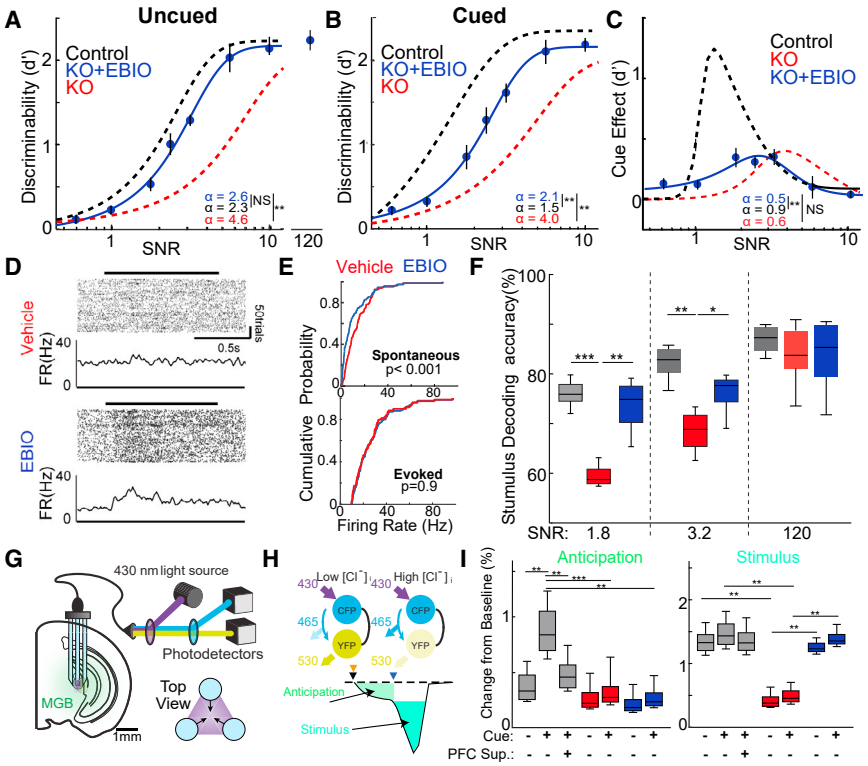

Figure 3. Restoring audTRN Function with EBIO Does Not Rescue the Executive Component of Cued Noisy Auditory Discrimination

(A) Task performance of KO mice injected with EBIO (blue; N = 6 mice; >14 sessions per condition) on uncued noise trials (performance of untreated control [black dotted line] and KO [red dotted line] mice shown for reference). EBIO administration significantly improved uncued performance, bringing it in line with controls (**p < 0.01; rank-sum test with Bonferroni correction).

(B) Task performance on cued trials were not fully rescued by EBIO administration in KO (blue; N = 6 mice; >14 sessions per condition) compared to control. Discrimination threshold and lapse rate were significantly increased compared to control (**p < 0.01; rank-sum test).

(C) Cue effect across SNR levels showing that the cue-related improvement in performance is not restored to control level (black dotted line shown for reference) by EBIO administration and is similar to untreated KO (red dotted line shown for reference). Cue-related change in discrimination threshold was significantly small compared to controls (**p < 0.01; rank-sum test).

(D) Example rasters and PSTHs for the same audTRN neuron recorded from a KO mouse following injection of vehicle (top) or EBIO (bottom).

(E) Cumulative probability plot of spontaneous (top) or sound-evoked (bottom) firing rates of audTRN neurons recorded in KO mice following vehicle (red) or EBIO (blue) injection (N = 3 KO mice, 168 KO neurons; Kolmogorov-Smirnov test).

(F) Poisson naive Bayes population decoding of MGBv responses to pure tones (20 kHz versus 24 kHz) with high (SNR 1.8), medium (SNR 3.2), or no (SNR 120) broadband noise added (see STAR Methods). EBIO (blue) improved population encoding in KO (red) to a level comparable to control (gray) for both noise conditions ($p < 5.2 \times 10^{-11}$ MANOVA; N = 3 control 4 KO mice; n = 424 control, 522 KO neurons; *p < 0.05; **p < 0.01; ***p < 0.001; rank-sum test).

(G) Schematic of improved chloride photometry setup used to measure thalamic inhibition in the MGBv via the fluorescent resonance energy transfer (FRET) indicator SuperClomeleon. A custom three terminal fiber was used for signal acquisition (see STAR Methods).

(H) (Top) Illustration of chloride-related fluorescence signal from the FRET indicator SuperClomeleon. This indicator contains a CFP donor and yellow fluorescent protein (YFP) acceptor. Elevated $[Cl^-]_i$ quenches YFP, reducing FRET signal. (Bottom) Diagram of distinct response components for an ideal single trial response in the cued noisy discrimination behavior is shown. Initiation (black arrow), cue presentation (orange arrow), and sound stimuli (blue arrow) are shown.

(I) Quantification of behavior-related inhibitory chloride signal response components in control (gray) and KO mice with vehicle (red) or EBIO (blue) injections. In uncued trials (bottom, left), a small increase in inhibitory signal was observed for anticipation. In control, this signal (gray) was increased by cue, an effect that was eliminated by PFC suppression (SNR = 1.8; N = 6 mice; >24 sessions per condition), but cue and PFC suppression did not affect the inhibitory signal during stimulus presentation. In KO, inhibitory signal (red) was diminished during both anticipation and stimulus period compared to control. EBIO selectively increased the chloride signal associated with stimulus response, but not anticipation (SNR = 3.2; $p < 8.3 \times 10^{-44}$ MANOVA; N = 6 mice; >16 sessions per condition; **p < 0.01; ***p < 0.001; rank-sum test).

Boxplots: median (line); quartiles (box); 95% confidence interval (whiskers). Error bars show SEM. See also Figure S3.

additional experiments to distinguish between these two hypotheses.

Restoration of audTRN Function Reveals an Executive Deficit in the KO

Our previous study indicated that deficits in thalamic sensory processing can be targeted by boosting SK channel activity, restoring sensory-evoked thalamic inhibitory responses in KO mice *in vivo* (Wells et al., 2016). As such, we assessed the impact of the SK channel positive allosteric modulator 1-ethyl-2-benzimidazolinOne (EBIO) (25 mg/kg) on task performance in KO mice. We found that EBIO injection resulted in near complete restoration of behavioral performance on trials in which no cue was delivered (Figure 3A). Intriguingly, however, this pharmacological approach had only a modest effect on cued trial performance (Figures 3B and 3C).

Is the lower effect on cued performance due to incomplete TRN pharmacological rescue or is it evidence for circuit perturbation beyond the TRN? To answer this question, we asked how EBIO delivery impacted neural measures of noise hypersensitivity in the KO. We found that EBIO ameliorated the elevated spontaneous spike rates we had observed in KO audTRN neurons (Figures 3D and 3E). Because sound-evoked responses remained similar (Figure 3E), this resulted in a restoration of audTRN dynamic range. In addition, firing rates in MGBv neurons were normalized (Figure S3A) and temporal response fidelity was improved (Figure S3B). Moreover, EBIO injection restored the ability to decode noise-masked pure tones used in the task based on population responses in the MGBv (Figure 3F).

In combination with our behavioral findings, these results indicated that, although EBIO largely normalized intrinsic thalamic circuitry in the context of auditory stimulus processing, this was insufficient for full behavioral rescue in cued noisy discrimination behavior. As such, we posited that the residual behavioral deficits might be due to dysfunction of circuits outside the TRN. Consistent with this notion, we found that PTCHD1 deletion largely limited to the TRN (Wells et al., 2016; see STAR Methods), resulting in animals that showed improvement on cued trials following EBIO injections that was comparable to controls (Figure S3C). Given previous findings showing that the cued component of this task involved stimulus-independent engagement of the audTRN (Nakajima et al., 2019), we next set out to test whether perturbation of executive control could explain residual deficits.

Previous studies (Nakajima et al., 2019; Wimmer et al., 2015) showed the PFC controls thalamic inhibition following cue onset but prior to target stimulus presentation. By developing a method to directly measure thalamic inhibition *in vivo* (see STAR Methods), we had been able to measure this anticipatory, PFC-dependent change in thalamic inhibition. Application of this method to the MGBv of both control and KO animals (Figure 3G) showed that EBIO rescued the sound-evoked thalamic inhibitory signal, but not its PFC-dependent engagement (Figures 3H and 3I), consistent with the idea that KO mice have an audTRN-independent deficit in the ability to engage filtering in response to a noise-predictive cue.

Prefrontal Encoding of Task-Relevant Cues Is Perturbed in the KO Mice

In a recent study, we had found that executive control of thalamic sensory filtering is implemented via a PFC-to-basal-ganglia-to-thalamus pathway capable of recruiting the sensory TRN (Nakajima et al., 2019). Based on the observed reduction in anticipatory, PFC-dependent thalamic inhibition in the KO, we considered that disruption of this control might produce the observed loss of executive control over sensory filtering. Because changes at later stages of this pathway could reflect deficits in "upstream" circuits, and because *Ptchd1* is expressed in the PFC of adult mice (Figure S4A), we first examined whether the PFC itself might be disrupted in the KO. As such, we recorded from PFC ensembles in these animals (Figure 4A) while they performed a slightly modified version of the cued noisy discrimination task. In this version, we introduced a second cue consisting of a different light color (UV or green randomly assigned for each animal; see STAR Methods) that did not reliably predict noise (unpredictive cue; 50% noise probability; see STAR Methods) to control for sensory responses to the cue. Previously, we showed that the unpredictive cue did not improve auditory discrimination behavior in control mice (Nakajima et al., 2019).

Although we did not observe a change in average spike rates between KOs and controls (Table S1) for putative excitatory (regular spiking [RS]) populations, several observations supported the notion that task-relevant activity in the PFC was disrupted in the KO. First, although some RS neurons in KO mice showed cueing-specific, temporally limited responses during the anticipation period consistent with those generally observed in control mice (Figure 4B; Nakajima et al., 2019), these responses did not reliably tile the delay period (Figure 4C). Indeed, the temporal distribution of these responses was skewed toward earlier times (Figure 4D), and significantly fewer were observed (Figure 4D, insets). Second, population decoding showed that encoding and maintenance of the predictive cue was reduced in KO animals (Figure 4E). Consistent with the notion that these effects were distinct from those observed in the audTRN, EBIO had no effect on peak numbers (Figure S4B) or rule encoding (Figure S4C).

The profile of task-related responses and the decoding time course suggested that KO mice might lack the ability to maintain a stable representation of the noise-predicting cue. Because previous studies had shown that cue maintenance relied on enhanced effective connectivity in the PFC, we wondered whether the apparent lack of representational stability in the KO might involve reduced connectivity. To address this question, we constructed a multi-neuronal generalized linear model (GLM) to predict the spike rate of each PFC neuron (Figure 4F; Park et al., 2014; Yates et al., 2017). The GLM model included coupling terms to capture the dependencies of spiking between neurons (see STAR Methods). Using this approach, we found that, although GLM coupling filters showed qualitatively similar temporal profiles (Figure 4G), the coupling strength, defined as the positive going response area, was reduced in the KO (Figures 4H and S4D). Importantly, EBIO did not rescue reduced effective connectivity, consistent with its primary impact being on sensory TRN physiology and supporting the notion that top-down control is a functionally dissociable deficit (Figure S4E).

Combined Targeting of TRN and Prefrontal Deficits in KO Mice Restores Behavior to Control Levels

Given the evidence for perturbation of task-relevant PFC functional connectivity in KO mice, we sought to develop a strategy to rescue it so as to alleviate deficits not targeted by EBIO. Because such deficits could be the result of intrinsic PFC dysfunction, dysfunction extrinsic to the PFC but relevant to its local functional connectivity, or both, we reasoned that our rescue strategy should focus on functional recovery rather than the exact underlying etiology of PFC functional connectivity deficits.

To correct PFC dysfunction, we considered a newly discovered role of the mediodorsal (MD) thalamus in enhancing local functional PFC connectivity (Bolkan et al., 2017; Halassa and Kastner, 2017; Halassa and Sherman, 2019; Nakajima and Halassa, 2017; Rikhye et al., 2018a, 2018b; Schmitt et al., 2017; Halassa, 2018), asking whether pharmacological agents known to activate the MD might enhance PFC functional connectivity. We found that modafinil was a prime candidate; it is a known cognitive enhancer with clinical efficacy in treating cognitive symptoms across a variety of disorders (Ford-Johnson et al., 2016; Wang et al., 2017) and improving psychomotor vigilance (Czeisler et al., 2005). Unlike classical stimulants, modafinil leads to improvement on a broad range of cognitive control tasks, particularly in attention deficit hyperactivity disorder (Minzenberg and Carter, 2008; Turner et al., 2004), a comorbidity often seen in Ptchd1 deletion patients (Chaudhry et al., 2015). Importantly, modafinil administration leads to

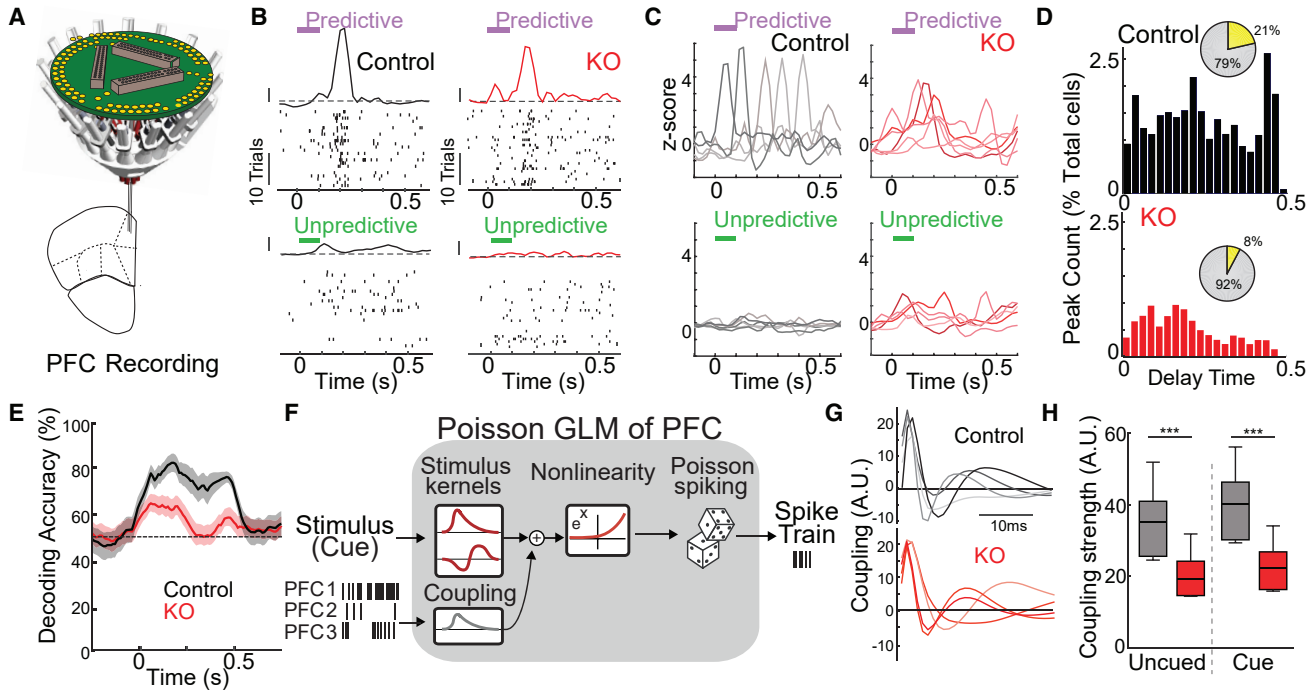

Figure 4. Maintenance of Cue Encoding in the PFC Is Disrupted in KO Mice

(A) Schematic of multi-electrode drive targeting the prelimbic region of frontal cortex (PFC).

(B) Example rasters and PSTHs of control (black, left) or KO (red, right) PFC neurons during the cued noisy discrimination task. To discriminate the PFC encoding of the meaning of noise-predictive cue from the sensory aspects of cue stimulus, we included noise unpredictive cues. Only correct trials are shown, separated according to the cueing condition. Zero time indicates cue presentation (100-ms duration; predictive cue, purple bar; unpredictive cue, green bar; PSTH scale bars: *Z* score = 1).

(C) Example PSTHs from 5 simultaneously recorded control (black, left) or KO (red, right) PFC neurons. KO neurons show predictive cue selective response peaks concentrated near the start of the delay.

(D) Distribution of peak times for control (top, black) or KO (bottom, red) mice as a percentage of total neurons showing distinct temporal profiles of peak concentration (totals for each genotype shown as inset pie charts; yellow, peak cells; $p < 0.01$; binomial test; N = 4 control, 4 KO mice; n = 863 control, 947 KO total neurons).

(E) Poisson naive Bayes decoding of predictive cue against unpredictive cue in control (gray) or KO (red) mice showing a significantly weaker and less stable encoding in the KO ($p < 8.5 \times 10^{-89}$; MANOVA; N = 4 control, 4 KO mice; n = 863 control, 947 KO neurons recorded). Decoding was limited to the 100 most strongly task-modulated cells in each trial set. Shaded region indicates 95% confidence intervals.

(F) Schematic of Poisson generalized linear model (GLM) used to model PFC spiking activity.

(G) Example of GLM-estimated coupling filters for PFC neurons in control (top) and KO (bottom) mice showing qualitatively similar coupling profiles across genotypes.

(H) Quantification of the positive coupling among regular spiking (RS) neurons in PFC of control (gray) and KO (red) mice during the delay period. Values shown include coupling for each neuron to all other simultaneously recorded neurons, averaged for each cell. Coupling was significantly reduced in the KO during both periods, suggesting that KO PFC exhibited reduced functional connectivity ($p < 1.3 \times 10^{-23}$; MANOVA; N = 4 control, 4 KO mice; n = 863 control, 947 KO neurons recorded; ***$p < 0.001$; rank-sum test).

Boxplots: median (line); quartiles (box); 95% confidence interval (whiskers). See also Figure S4 and Table S1.

preferential c-*fos* expression and positron emission tomography (PET) signals in rat MD thalamus (Gozzi et al., 2012) and enhanced blood-oxygen-level-dependent (BOLD) signals in human MD (Schmaal et al., 2013).

Consistent with these reports, we found that injection of modafinil (13 mg/kg) in control mice increased spike rates in MD thalamus (Figures S5A and S5B). More importantly, modafinil augmented responses to optogenetic stimulation of intra-PFC connections (Figures 5A–5C), a direct measure of effective connectivity (Schmitt et al., 2017). Strikingly, optogenetic suppression of the MD selectively impacted this measure, reducing stimulated responses during administration of vehicle and eliminating the increase normally associated with modafinil (Figures 5D, 5E, and S5C) without impacting increased baseline spike due to modafinil administration (Figure S5D).

Could modafinil rescue deficient task-relevant functional connectivity and restore normal PFC function in the KO? To see whether we could answer this question using multi-neuronal GLM coupling filters (Park et al., 2014), we initially determined whether this method could measure relevant changes in connectivity by assessing coupling changes produced by MD suppression with and without modafinil. We found that the changes in coupling strength produced by modafinil and MD suppression mirrored those measured using our connectivity

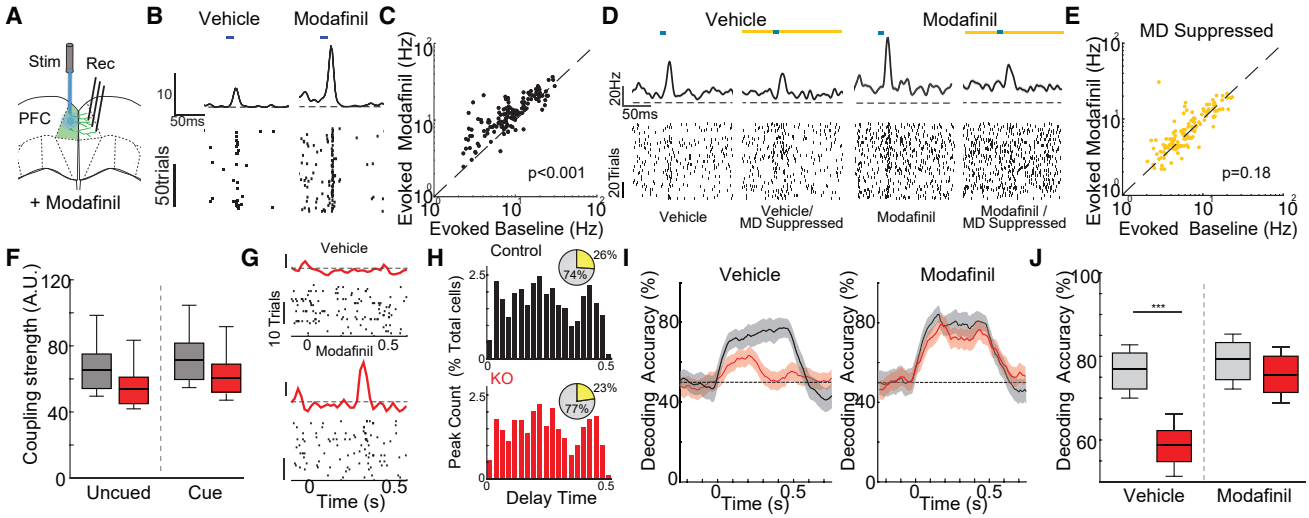

Figure 5. Modafinil Restores Cue Encoding in the KO PFC

(A) Cartoon illustrating the approach used to measure intra-PFC connectivity via optical stimulation.

(B) The evoked response of a PFC neuron to intra-PFC stimulation (blue bar) is much stronger with modafinil injection.

(C) Modafinil significantly increased the strength of evoked peak responses, demonstrating that modafinil can increase intra-PFC connectivity (N = 2 mice; n = 155 neurons; sign-rank test).

(D) Example rasters and PSTHs from a PFC neuron showing that the effect of modafinil on stimulated intra-PFC connections (blue bar) disappeared when MD was silenced (yellow bar).

(E) Modafinil effects on intra-PFC connectivity disappeared with MD suppression (N = 2 mice; n = 155 neurons; sign-rank test).

(F) Quantification of the positive coupling strengths in the PFC of control (gray) and KO (red) mice during the delay period with or without modafinil. Modafinil restored connectivity to control levels in the KO ($p < 1.3 \times 10^{-23}$; MANOVA; N = 4 control, 4 KO mice; n = 863 control, 947 KO neurons recorded; rank-sum test).

(G) Example rasters and PSTHs of a KO PFC neuron during delay of the cued noisy auditory discrimination task following injection of vehicle (top) or modafinil (bottom). Following modafinil administration, a new task-related response peak was observed (scale bars: *Z* score = 1).

(H) Distribution of peak times for control (top, black) or KO (bottom, red) mice following modafinil injection as a percentage of total neurons. Peak numbers and temporal distribution were comparable between control and KO following modafinil administration (totals for each genotype shown as inset pie charts; yellow, peak cells; $p < 0.01$; KO modafinil versus vehicle non-significant for KO versus control with modafinil binomial test; N = 4 control, 4 KO mice; n = 863 control, 947 KO neurons).

(I) Poisson naive Bayes decoding of predictive cue against unpredictive cue in control (gray) or KO (red) mice showing that modafinil (right) significantly increased cue encoding in the KO compared with vehicle (left). Shaded region indicates 95% confidence intervals.

(J) Quantification of the comparisons of decoding with and without modafinil shown in (I) ($p < 8.5 \times 10^{-89}$; MANOVA; N = 4 control, 4 KO mice; n = 863 control, 947 KO neurons recorded; ***$p < 0.001$; binomial test).

Boxplots: median (line); quartiles (box); 95% confidence interval (whiskers). See also Figure S5.

assay. Furthermore, GLM estimates were able to detect the MD-suppression-dependent elimination of changes in coupling normally produced by modafinil (Figures S5C and S5E). With these validations in hand, we applied this method to assess how modafinil impacted PFC functional connectivity in the KO during behavior. We found that modafinil significantly increased coupling strength in the KO (Figure S5F), normalizing it to control levels (Figures 5F and S5G). Consistent with the idea that deficits in connectivity produced the observed instability of PFC encoding, injection of modafinil increased the number of transient responses, particularly at long delays (Figures 5G and 5H), and restored stable encoding and maintenance of noise predictive cue in the KO PFC (Figures 5I and 5J).

The observed improvement in PFC function produced by modafinil suggested that it could be part of a rescue strategy for the noise filtering deficits in the KO. Indeed, we found that modafinil administration significantly enhanced KO performance on the noisy discrimination auditory Go/No Go task but that such enhancement was limited to cued trials and stimulus SNR of >3 (Figures 6A–6C). In fact, unlike EBIO, modafinil had no impact on behavioral performance when no noise-predictive cue was provided. If the modafinil improved behavior through MD instead of audTRN, we reasoned that MD suppression would diminish this cue-dependent effect. Consistent with this idea, we found that the enhanced cue effect normally produced by the modafinil was absent when MD was suppressed (Figure S6A). In line with the idea that modafinil worked on a pathway separate from automatic noise filtering via the audTRN, we also found that it selectively enhanced the anticipatory photometry signal in the MGBv, an effect opposite to what we had observed following EBIO administration (Figure 6D compared with Figure 3I).

Given such non-overlapping effects of modafinil and EBIO, we wondered whether their complementary benefits might completely rescue behavioral deficits in the KO. This was indeed the case as combining modafinil and EBIO resulted in near-complete behavioral rescue of auditory noise sensitivity in KO mice,

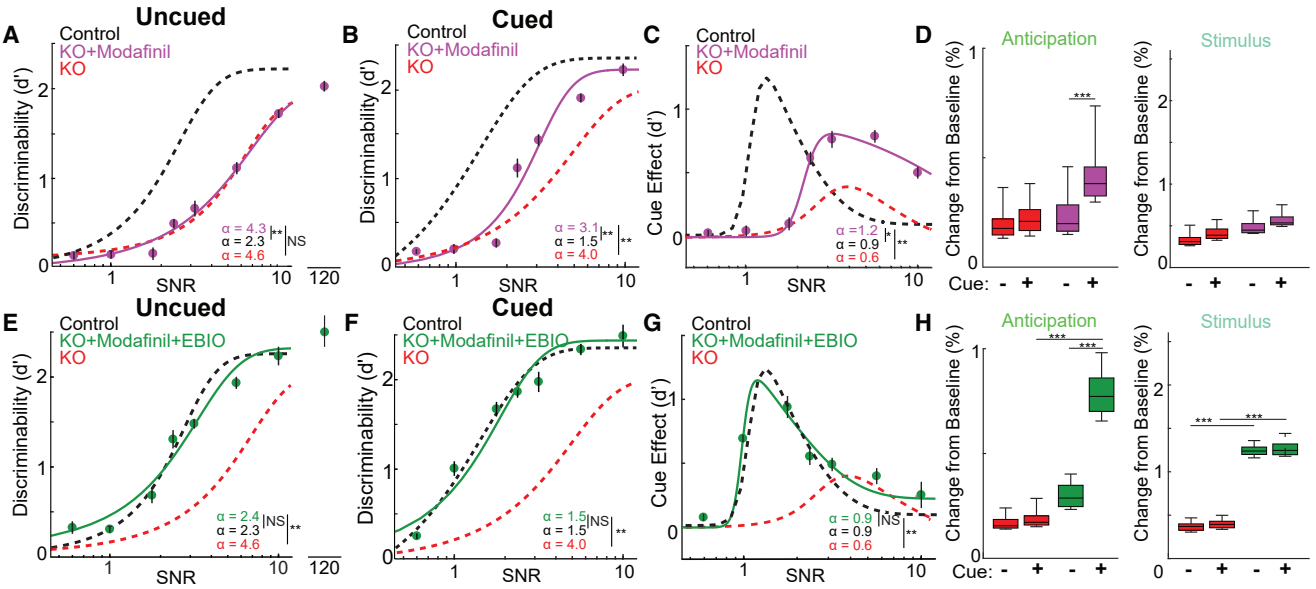

Figure 6. Combining Modafinil and EBIO Restores PFC and audTRN Function to Rescue Discrimination Performance in the KO

(A) Discrimination threshold and lapse rate for KO mice with modafinil (purple; N = 6 mice; >14 sessions per condition) were unchanged compared with untreated KO (**p < 0.01; rank-sum test).

(B) Modafinil produced selective improvements on predictive cue noise trials with SNR > 3 in KO mice (purple; N = 6 mice; >14 sessions per condition; **p < 0.01; rank-sum test).

(C) Despite some improvement after modafinil (purple; N = 6 mice; >14 sessions per condition) compared with non-drug conditions, the cue effect was not restored to control levels and the cue-related change in discrimination threshold remained lower (*p < 0.05; **p < 0.01; rank-sum test).

(D) Quantification of behavior-related inhibitory chloride signal response components (Figure 3H) in KO mice with vehicle (red) or modafinil (purple) injections. Modafinil increased the chloride signal associated with anticipation (SNR = 3.2; $p < 1.4 \times 10^{-64}$; MANOVA; N = 6 mice; >16 sessions per condition; **p < 0.01; ***p < 0.001; rank-sum test).

(E) Combination of modafinil and EBIO (green; N = 6 mice; >10 session per condition) fully rescued behavioral deficits in KO for uncued trials leading to performance comparable to controls (**p < 0.01; rank-sum test).

(F) Combination of modafinil and EBIO fully rescued behavioral deficits in KO for cued trials (green; N = 6 mice; >10 sessions per condition; **p < 0.01; rank-sum test).

(G) Following combined treatment (green), the cue effect was qualitatively similar to controls and the cue-related change in discrimination threshold was significantly increased (**p < 0.01; rank-sum test; N = 6 mice; >10 sessions per condition).

(H) Quantification of behavior-related inhibitory chloride signal response components in KO mice with vehicle (red) or KO injected with both modafinil and EBIO (green) injections. The combined treatment increased the chloride signal associated with both anticipation and stimulus response to control levels (SNR = 1.8; $p < 7.5 \times 10^{-68}$; MANOVA; N = 6 mice; >16 sessions per condition; ***p < 0.001; rank-sum test).

Boxplots: median (line); quartiles (box); 95% confidence interval (whiskers). Error bars show SEM. See also Figure S6.

both in cued and uncued trials (Figures 6E–6G). In addition, behavioral rescue was associated with restoration of control-like MGBv inhibitory photometry signals (Figure 6H), suggesting that behavioral improvement was a result of correcting deficits in the intrinsic function and executive control of the audTRN. Overall, by characterizing and targeting multiple circuit defects in a distributed network that supports sensory filtering, we were able to fully rescue noise hypersensitivity in the PTCHD1 KO model of human ASD.

DISCUSSION

In this study, we used a targeted combination of approaches to identify multiple deficits in a distributed forebrain network that produced disrupted sensory filtering in a mouse model of ASD, the PTCHD1 KO. These findings enabled development of a combinatorial treatment targeting multiple circuits that allowed us to fully rescue noise hypersensitivity in this model. Overall, our results highlight how investigating neurodevelopmental disorders from the perspective of functional circuit architecture can facilitate identification of treatments to correct symptoms in these complex disorders.

Impact and Basis of Reduced audTRN Dynamic Range

Although the mechanism underlying changes in audTRN function in the KO is unknown, our previous results suggest that it involves reduced activity of SK channels (Wells et al., 2016). Blockade of these channels in some cell types leads to higher basal firing rates (Abbasi et al., 2016; Deister et al., 2009), consistent with the change we observe in KO audTRN neurons, an effect that was mitigated by the SK allosteric modulator EBIO. Due to high baseline activity, KO audTRN neurons are near response saturation, resulting in diminished sound-driven responses.

In contrast to audTRN neurons, MGBv sensory responses were elevated in the KO and also showed a loss of response

fidelity. These finding suggest that smaller sound-driven audTRN responses result in a loss in effective inhibition in the MGBv. This implies that MGBv neurons are sensitive to changes in audTRN spiking, possibly because of desensitization to chronic inhibitory input (Deeb et al., 2013; Hines et al., 2012; Saliba et al., 2007; Thompson and Gähwiler, 1989). Sensitivity to rapid audTRN dynamics would also explain the impact of EBIO on the MGBv. By reducing baseline firing rates in audTRN neurons, EBIO restores sound-evoked audTRN responses, allowing it to suppress MGBv.

Multiple Circuit Basis of Abnormal Auditory Processing in Ptchd1 KO

Because we have not examined all stages of auditory processing, we cannot completely rule out that changes outside the TRN and PFC contribute to deficits in the KO. However, changes in activity we observe are inconsistent with abnormalities in peripheral auditory processing alone, because these would result in similar firing rate changes in audTRN and MGBv. Disruption of A1 function should also impact audTRN and MGBv similarly, as A1 projections go to both circuits. In addition, the rescue of behavioral noise hypersensitivity by EBIO in the SOM-Cre × Ptchd1 TRN-specific KO supports the idea that disrupted audTRN activity is a key contributor to abnormal sensory processing in the full KO. Together, these observations support the notion that changes in audTRN function best explain abnormalities in sensory filtering that we observe in behavior.

Correcting Cortical Connectivity Deficits in the PFC as a Treatment in ASD

Noise hypersensitivity is a major symptom of ASD that profoundly affects patients' ability to cope with their environment (Wiggins et al., 2009). This symptom is highly prevalent, with 65% of patients reporting a sensitivity to distracting stimuli (Bishop and Seltzer, 2012; Tomchek and Dunn, 2007). Our results indicate that, in addition to problems in low-level filtering, this hypersensitivity may involve dysfunction in PFC-dependent control. Consistent with this idea, postmortem analysis of brain tissue has identified abnormalities in prefrontal cell properties (Courchesne et al., 2011) and transcriptional profile in ASD (Voineagu et al., 2011). Abnormal engagement of the PFC in tasks requiring attention and other executive functions is also observed in ASD (Just et al., 2007). Investigation of mouse models of ASD has also suggested abnormal dynamics occur in the PFC (Bey et al., 2018; Luongo et al., 2016).

We found that EBIO did not rescue PFC dysfunction in the KO, suggesting that the dysfunction does not involve reduced SK channel currents. This is consistent with the lack of firing rate increase in the KO PFC, because SK current reduction would be expected to increase firing rate (Criado-Marrero et al., 2014). On the other hand, modafinil did improve PFC function. The complex pharmacology of modafinil makes it difficult to identify how it rescues function, but it appears to involve enhancement of effective connectivity in the PFC due to increased activity in the MD. Understanding the nature of modafinil's influence will be useful in identifying other interventions to improve PFC function in ASD.

Benefits of a Circuit-Function-Based Approach to Disease

One of the most significant translational findings over the last decade has been the elucidation of common molecular, cellular, and circuit disruptions across seemingly distinct neurodevelopmental disorders (Coe et al., 2012a, 2012b). Molecular analysis of ASD, schizophrenia, and attention-deficit hyperactivity disorder (ADHD) shows substantial overlap in the genes disrupted (Cristino et al., 2014). The diverse symptoms of these disorders reinforce the notion that neither clinical phenomenology nor genetic characterization alone can capture their etiology (Casey et al., 2014; Insel et al., 2010; Insel, 2014; Krol et al., 2018; Schmitt and Halassa, 2017). Unfortunately, an approach to define functional connections between these levels disease characterization is lacking.

Our findings identify multiple circuit substrates of sensory filtering that are disrupted in the Ptchd1 KO. The relevance of these circuits to disease is unlikely to be limited to cases in which Ptchd1 is mutated. Indeed, disease-relevant mutations affecting any of the circuits recently identified to be involved in noise filtering (PFC, striatum, GP, or audTRN; Nakajima et al., 2019) would likely produces similar deficits. For example, defects in cortical-striatum circuits in Shank3 mutant mice (Peça et al., 2011) could explain hypersensitivity found in patients with mutations of this gene (Moessner et al., 2007). Similarly, mutation of CNTNAP2, which may disrupt PFC function (Selimbeyoglu et al., 2017), leads to hyper-reactivity to stimuli (Peñagarikano et al., 2011). This suggests that circuit dysfunctions like those identified in this study could explain sensory processing deficits in multiple forms of ASD, providing a potentially valuable new strategic direction in developing novel treatments.

STAR★METHODS

Detailed methods are provided in the online version of this paper and include the following:

- KEY RESOURCES TABLE
- LEAD CONTACT AND MATERIALS AVAILABILITY
- EXPERIMENTAL MODEL AND SUBJECT DETAILS
- METHOD DETAILS
  - Behavioral Training and Testing
  - Behavioral Analysis
  - Optical Chloride Measurements in Behavior
  - Virus Set and Injection Coordinates
  - Optic fiber Implantation
  - Microdrive Array Construction and Implantation
  - Head Fixation and Stimulus Delivery System
  - Electrophysiological Recordings
  - Connectivity Assay
  - Fano Factor
  - Identification of peaks in task-modulated neurons
  - Decoding Analysis
  - Generalized Linear Model Based Coupling Estimation
  - Pharmacological Manipulations
  - Slice Recordings

SUPPLEMENTAL INFORMATION

Supplemental Information can be found online at https://doi.org/10.1016/j.neuron.2019.09.040.

ACKNOWLEDGMENTS

We thank S.N. Oline and M. Wells for technical assistance. M.M.H. is supported by the Simons Center for the Social Brain at MIT, the Stanley Center for Psychiatric Research at the Broad Institute, the McGovern Institute for Brain Research at MIT, the Pew Foundation, the Human Frontiers Science Program, and NIH grants R01NS098505 and R01MH107680. G.F. is supported by the Simons Center for the Social Brain at MIT, the James and Patricia Poitras Center for Psychiatric Disorders Research at MIT, the Hock E. Tan and K. Lisa Yang Center for Autism Research at MIT, the Stanley Center for Psychiatric Research at the Broad Institute of MIT and Harvard, and NIH/NINDS grant R01NS098505. M.N. is supported by a JSPS fellowship. L.I.S. is supported by a NARSAD Young Investigator Award.

AUTHOR CONTRIBUTIONS

M.N., L.I.S., and M.M.H. conceived experiments and analyses, interpreted the data, and wrote the manuscript. M.N. and L.I.S. performed behavioral, optical, and electrophysiological experiments and analyzed the data. G.F. provided Ptchd1 KO mice. M.M.H. supervised the experiment and directed the analysis. All authors read the final version of the manuscript.

DECLARATION OF INTERESTS

The authors declare no competing interests.

Received: May 13, 2019
Revised: September 3, 2019
Accepted: September 23, 2019
Published: October 21, 2019

REFERENCES

Abbasi, S., Abbasi, A., Sarbaz, Y., and Shahabi, P. (2016). Contribution of somatic and dendritic SK channels in the firing rate of deep cerebellar nuclei: implication in cerebellar ataxia. Basic Clin. Neurosci. *7*, 57–61.

Anderson, L.A., Christianson, G.B., and Linden, J.F. (2009). Stimulus-specific adaptation occurs in the auditory thalamus. J. Neurosci. *29*, 7359–7363.

Baum, S.H., Stevenson, R.A., and Wallace, M.T. (2015). Behavioral, perceptual, and neural alterations in sensory and multisensory function in autism spectrum disorder. Prog. Neurobiol. *134*, 140–160.

Bey, A.L., Wang, X., Yan, H., Kim, N., Passman, R.L., Yang, Y., Cao, X., Towers, A.J., Hulbert, S.W., Duffney, L.J., et al. (2018). Brain region-specific disruption of Shank3 in mice reveals a dissociation for cortical and striatal circuits in autism-related behaviors. Transl. Psychiatry *8*, 94.

Bishop, S.L., and Seltzer, M.M. (2012). Self-reported autism symptoms in adults with autism spectrum disorders. J. Autism Dev. Disord. *42*, 2354–2363.

Bolkan, S.S., Stujenske, J.M., Parnaudeau, S., Spellman, T.J., Rauffenbart, C., Abbas, A.I., Harris, A.Z., Gordon, J.A., and Kellendonk, C. (2017). Thalamic projections sustain prefrontal activity during working memory maintenance. Nat. Neurosci. *20*, 987–996.

Casey, B.J., Oliveri, M.E., and Insel, T. (2014). A neurodevelopmental perspective on the research domain criteria (RDoC) framework. Biol. Psychiatry *76*, 350–353.

Chaudhry, A., Noor, A., Degagne, B., Baker, K., Bok, L.A., Brady, A.F., Chitayat, D., Chung, B.H., Cytrynbaum, C., Dyment, D., et al.; DDD Study (2015). Phenotypic spectrum associated with PTCHD1 deletions and truncating mutations includes intellectual disability and autism spectrum disorder. Clin. Genet. *88*, 224–233.

Chung, J.E., Magland, J.F., Barnett, A.H., Tolosa, V.M., Tooker, A.C., Lee, K.Y., Shah, K.G., Felix, S.H., Frank, L.M., and Greengard, L.F. (2017). A fully automated approach to spike sorting. Neuron *95*, 1381–1394.e6.

Churchland, M.M., Yu, B.M., Cunningham, J.P., Sugrue, L.P., Cohen, M.R., Corrado, G.S., Newsome, W.T., Clark, A.M., Hosseini, P., Scott, B.B., et al. (2010). Stimulus onset quenches neural variability: a widespread cortical phenomenon. Nat. Neurosci. *13*, 369–378.

Coe, B.P., Girirajan, S., and Eichler, E.E. (2012a). A genetic model for neurodevelopmental disease. Curr. Opin. Neurobiol. *22*, 829–836.

Coe, B.P., Girirajan, S., and Eichler, E.E. (2012b). The genetic variability and commonality of neurodevelopmental disease. Am. J. Med. Genet. C. Semin. Med. Genet. *160C*, 118–129.

Cotillon-Williams, N., Huetz, C., Hennevin, E., and Edeline, J.M. (2008). Tonotopic control of auditory thalamus frequency tuning by reticular thalamic neurons. J. Neurophysiol. *99*, 1137–1151.

Courchesne, E., Mouton, P.R., Calhoun, M.E., Semendeferi, K., Ahrens-Barbeau, C., Hallet, M.J., Barnes, C.C., and Pierce, K. (2011). Neuron number and size in prefrontal cortex of children with autism. JAMA *306*, 2001–2010.

Crabtree, J.W. (1999). Intrathalamic sensory connections mediated by the thalamic reticular nucleus. Cell. Mol. Life Sci. *56*, 683–700.

Crabtree, J.W. (2018). Functional diversity of thalamic reticular subnetworks. Front. Syst. Neurosci. *12*, 41.

Criado-Marrero, M., Santini, E., and Porter, J.T. (2014). Modulating fear extinction memory by manipulating SK potassium channels in the infralimbic cortex. Front. Behav. Neurosci. *8*, 96.

Cristino, A.S., Williams, S.M., Hawi, Z., An, J.Y., Bellgrove, M.A., Schwartz, C.E., Costa, Lda.F., and Claudianos, C. (2014). Neurodevelopmental and neuropsychiatric disorders represent an interconnected molecular system. Mol. Psychiatry *19*, 294–301.

Cruikshank, S.J., Urabe, H., Nurmikko, A.V., and Connors, B.W. (2010). Pathway-specific feedforward circuits between thalamus and neocortex revealed by selective optical stimulation of axons. Neuron *65*, 230–245.

Cueni, L., Canepari, M., Luján, R., Emmenegger, Y., Watanabe, M., Bond, C.T., Franken, P., Adelman, J.P., and Lüthi, A. (2008). T-type Ca2+ channels, SK2 channels and SERCAs gate sleep-related oscillations in thalamic dendrites. Nat. Neurosci. *11*, 683–692.

Czeisler, C.A., Walsh, J.K., Roth, T., Hughes, R.J., Wright, K.P., Kingsbury, L., Arora, S., Schwartz, J.R., Niebler, G.E., and Dinges, D.F.; U.S. Modafinil in Shift Work Sleep Disorder Study Group (2005). Modafinil for excessive sleepiness associated with shift-work sleep disorder. N. Engl. J. Med. *353*, 476–486.

Deeb, T.Z., Nakamura, Y., Frost, G.D., Davies, P.A., and Moss, S.J. (2013). Disrupted Cl(-) homeostasis contributes to reductions in the inhibitory efficacy of diazepam during hyperexcited states. Eur. J. Neurosci. *38*, 2453–2467.

Deister, C.A., Chan, C.S., Surmeier, D.J., and Wilson, C.J. (2009). Calcium-activated SK channels influence voltage-gated ion channels to determine the precision of firing in globus pallidus neurons. J. Neurosci. *29*, 8452–8461.

Dhingra, N.K., and Smith, R.G. (2004). Spike generator limits efficiency of information transfer in a retinal ganglion cell. J. Neurosci. *24*, 2914–2922.

Duda, R.O., Hart, P.E., and Stork, D.G. (2001). Pattern Classification, Second Edition (Wiley).

Dunn, F.A., Doan, T., Sampath, A.P., and Rieke, F. (2006). Controlling the gain of rod-mediated signals in the Mammalian retina. J. Neurosci. *26*, 3959–3970.

Filges, I., Röthlisberger, B., Blattner, A., Boesch, N., Demougin, P., Wenzel, F., Huber, A.R., Heinimann, K., Weber, P., and Miny, P. (2011). Deletion in

Xp22.11: PTCHD1 is a candidate gene for X-linked intellectual disability with or without autism. Clin. Genet. *79*, 79–85.

Ford-Johnson, L., DeLuca, J., Zhang, J., Elovic, E., Lengenfelder, J., and Chiaravalloti, N.D. (2016). Cognitive effects of modafinil in patients with multiple sclerosis: a clinical trial. Rehabil. Psychol. *61*, 82–91.

Gozzi, A., Colavito, V., Seke Etet, P.F., Montanari, D., Fiorini, S., Tambalo, S., Bifone, A., Zucconi, G.G., and Bentivoglio, M. (2012). Modulation of fronto-cortical activity by modafinil: a functional imaging and fos study in the rat. Neuropsychopharmacology *37*, 822–837.

Hackett, T.A., Barkat, T.R., O'Brien, B.M., Hensch, T.K., and Polley, D.B. (2011). Linking topography to tonotopy in the mouse auditory thalamocortical circuit. J. Neurosci. *31*, 2983–2995.

Halassa, M.M. (2018). Fronto-thalamic architectures for cognitive algorithms. Neuron *98*, 237–239.

Halassa, M.M., and Acsády, L. (2016). Thalamic inhibition: diverse sources, diverse scales. Trends Neurosci. *39*, 680–693.

Halassa, M.M., and Kastner, S. (2017). Thalamic functions in distributed cognitive control. Nat. Neurosci. *20*, 1669–1679.

Halassa, M.M., and Sherman, S.M. (2019). Thalamocortical circuit motifs: a general framework. Neuron *103*, 762–770.

Halassa, M.M., Chen, Z., Wimmer, R.D., Brunetti, P.M., Zhao, S., Zikopoulos, B., Wang, F., Brown, E.N., and Wilson, M.A. (2014). State-dependent architecture of thalamic reticular subnetworks. Cell *158*, 808–821.

Hines, R.M., Davies, P.A., Moss, S.J., and Maguire, J. (2012). Functional regulation of GABAA receptors in nervous system pathologies. Curr. Opin. Neurobiol. *22*, 552–558.

Hromádka, T., and Zador, A.M. (2009). Representations in auditory cortex. Curr. Opin. Neurobiol. *19*, 430–433.

Insel, T.R. (2014). The NIMH Research Domain Criteria (RDoC) Project: precision medicine for psychiatry. Am. J. Psychiatry *171*, 395–397.

Insel, T., Cuthbert, B., Garvey, M., Heinssen, R., Pine, D.S., Quinn, K., Sanislow, C., and Wang, P. (2010). Research domain criteria (RDoC): toward a new classification framework for research on mental disorders. Am. J. Psychiatry *167*, 748–751.

Intaitė, M., Georgescu, A.L., Noreika, V., von Saldern, M.A., Vogeley, K., and Falter-Wagner, C.M. (2019). Adults with autism spectrum condition have atypical perception of ambiguous figures when bottom-up and top-down interactions are incongruous. Autism *23*, 1133–1142.

Jadi, M., Polsky, A., Schiller, J., and Mel, B.W. (2012). Location-dependent effects of inhibition on local spiking in pyramidal neuron dendrites. PLoS Comput. Biol. *8*, e1002550.

Juavinett, A.L., Erlich, J.C., and Churchland, A.K. (2018). Decision-making behaviors: weighing ethology, complexity, and sensorimotor compatibility. Curr. Opin. Neurobiol. *49*, 42–50.

Just, M.A., Cherkassky, V.L., Keller, T.A., Kana, R.K., and Minshew, N.J. (2007). Functional and anatomical cortical underconnectivity in autism: evidence from an FMRI study of an executive function task and corpus callosum morphometry. Cereb. Cortex *17*, 951–961.

Kato, S., Kobayashi, K., Inoue, K., Kuramochi, M., Okada, T., Yaginuma, H., Morimoto, K., Shimada, T., Takada, M., and Kobayashi, K. (2011). A lentiviral strategy for highly efficient retrograde gene transfer by pseudotyping with fusion envelope glycoprotein. Hum. Gene Ther. *22*, 197–206.

Krol, A., Wimmer, R.D., Halassa, M.M., and Feng, G. (2018). Thalamic reticular dysfunction as a circuit endophenotype in neurodevelopmental disorders. Neuron *98*, 282–295.

Liang, L., Oline, S.N., Kirk, J.C., Schmitt, L.I., Komorowski, R.W., Remondes, M., and Halassa, M.M. (2017). Scalable, lightweight, integrated and quick-to-assemble (SLIQ) hyperdrives for functional circuit dissection. Front. Neural Circuits *11*, 8.

Liss, M., Saulnier, C., Fein, D., and Kinsbourne, M. (2006). Sensory and attention abnormalities in autistic spectrum disorders. Autism *10*, 155–172.

Luongo, F.J., Horn, M.E., and Sohal, V.S. (2016). Putative microcircuit-level substrates for attention are disrupted in mouse models of autism. Biol. Psychiatry *79*, 667–675.

Luque, M.A., Beltran-Matas, P., Marin, M.C., Torres, B., and Herrero, L. (2017). Excitability is increased in hippocampal CA1 pyramidal cells of Fmr1 knockout mice. PLoS ONE *12*, e0185067.

Marco, E.J., Hinkley, L.B., Hill, S.S., and Nagarajan, S.S. (2011). Sensory processing in autism: a review of neurophysiologic findings. Pediatr. Res. *69*, 48R–54R.

Marshall, C.R., Noor, A., Vincent, J.B., Lionel, A.C., Feuk, L., Skaug, J., Shago, M., Moessner, R., Pinto, D., Ren, Y., et al. (2008). Structural variation of chromosomes in autism spectrum disorder. Am. J. Hum. Genet. *82*, 477–488.

Meyers, E.M. (2013). The neural decoding toolbox. Front. Neuroinform. *7*, 8.

Miles, R., Tóth, K., Gulyás, A.I., Hájos, N., and Freund, T.F. (1996). Differences between somatic and dendritic inhibition in the hippocampus. Neuron *16*, 815–823.

Minzenberg, M.J., and Carter, C.S. (2008). Modafinil: a review of neurochemical actions and effects on cognition. Neuropsychopharmacology *33*, 1477–1502.

Mitchell, S.J., and Silver, R.A. (2003). Shunting inhibition modulates neuronal gain during synaptic excitation. Neuron *38*, 433–445.

Mitchell, T.M., Hutchinson, R., Niculescu, R.S., Pereira, F., Wang, X., Just, M., and Newman, S. (2004). Learning to decode cognitive states from brain images. Mach. Learn. *57*, 145–175.

Moessner, R., Marshall, C.R., Sutcliffe, J.S., Skaug, J., Pinto, D., Vincent, J., Zwaigenbaum, L., Fernandez, B., Roberts, W., Szatmari, P., and Scherer, S.W. (2007). Contribution of SHANK3 mutations to autism spectrum disorder. Am. J. Hum. Genet. *81*, 1289–1297.

Mortensen, U. (2002). Additive noise, Weibull functions and the approximation of psychometric functions. Vision Res. *42*, 2371–2393.

Nakajima, M., and Halassa, M.M. (2017). Thalamic control of functional cortical connectivity. Curr. Opin. Neurobiol. *44*, 127–131.

Nakajima, M., Schmitt, L.I., and Halassa, M.M. (2019). Prefrontal cortex regulates sensory filtering through a basal ganglia-to-thalamus pathway. Neuron *103*, 445–458.e10.

Noor, A., Whibley, A., Marshall, C.R., Gianakopoulos, P.J., Piton, A., Carson, A.R., Orlic-Milacic, M., Lionel, A.C., Sato, D., Pinto, D., et al.; Autism Genome Project Consortium (2010). Disruption at the PTCHD1 Locus on Xp22.11 in autism spectrum disorder and intellectual disability. Sci. Transl. Med. *2*, 49ra68.

Ostojic, S., and Brunel, N. (2011). From spiking neuron models to linear-nonlinear models. PLoS Comput. Biol. *7*, e1001056.

Overath, T., McDermott, J.H., Zarate, J.M., and Poeppel, D. (2015). The cortical analysis of speech-specific temporal structure revealed by responses to sound quilts. Nat. Neurosci. *18*, 903–911.

Park, I.M., Meister, M.L., Huk, A.C., and Pillow, J.W. (2014). Encoding and decoding in parietal cortex during sensorimotor decision-making. Nat. Neurosci. *17*, 1395–1403.

Peça, J., Feliciano, C., Ting, J.T., Wang, W., Wells, M.F., Venkatraman, T.N., Lascola, C.D., Fu, Z., and Feng, G. (2011). Shank3 mutant mice display autistic-like behaviours and striatal dysfunction. Nature *472*, 437–442.

Peñagarikano, O., Abrahams, B.S., Herman, E.I., Winden, K.D., Gdalyahu, A., Dong, H., Sonnenblick, L.I., Gruver, R., Almajano, J., Bragin, A., et al. (2011). Absence of CNTNAP2 leads to epilepsy, neuronal migration abnormalities, and core autism-related deficits. Cell *147*, 235–246.

Pillow, J.W., Paninski, L., Uzzell, V.J., Simoncelli, E.P., and Chichilnisky, E.J. (2005). Prediction and decoding of retinal ganglion cell responses with a probabilistic spiking model. J. Neurosci. *25*, 11003–11013.

Pillow, J.W., Shlens, J., Paninski, L., Sher, A., Litke, A.M., Chichilnisky, E.J., and Simoncelli, E.P. (2008). Spatio-temporal correlations and visual signalling in a complete neuronal population. Nature *454*, 995–999.

Pinault, D. (2004). The thalamic reticular nucleus: structure, function and concept. Brain Res. Brain Res. Rev. *46*, 1–31.

Pinto, D., Pagnamenta, A.T., Klei, L., Anney, R., Merico, D., Regan, R., Conroy, J., Magalhaes, T.R., Correia, C., Abrahams, B.S., et al. (2010). Functional impact of global rare copy number variation in autism spectrum disorders. Nature *466*, 368–372.

Rikhye, R.V., Gilra, A., and Halassa, M.M. (2018a). Thalamic regulation of switching between cortical representations enables cognitive flexibility. Nat. Neurosci. *21*, 1753–1763.

Rikhye, R.V., Wimmer, R.D., and Halassa, M.M. (2018b). Toward an integrative theory of thalamic function. Annu. Rev. Neurosci. *41*, 163–183.

Saliba, R.S., Michels, G., Jacob, T.C., Pangalos, M.N., and Moss, S.J. (2007). Activity-dependent ubiquitination of GABA(A) receptors regulates their accumulation at synaptic sites. J. Neurosci. *27*, 13341–13351.

Schmaal, L., Joos, L., Koeleman, M., Veltman, D.J., van den Brink, W., and Goudriaan, A.E. (2013). Effects of modafinil on neural correlates of response inhibition in alcohol-dependent patients. Biol. Psychiatry *73*, 211–218.

Schmitt, L.I., and Halassa, M.M. (2017). Interrogating the mouse thalamus to correct human neurodevelopmental disorders. Mol. Psychiatry *22*, 183–191.

Schmitt, L.I., Wimmer, R.D., Nakajima, M., Happ, M., Mofakham, S., and Halassa, M.M. (2017). Thalamic amplification of cortical connectivity sustains attentional control. Nature *545*, 219–223.

Selimbeyoglu, A., Kim, C.K., Inoue, M., Lee, S.Y., Hong, A.S.O., Kauvar, I., Ramakrishnan, C., Fenno, L.E., Davidson, T.J., Wright, M., and Deisseroth, K. (2017). Modulation of prefrontal cortex excitation/inhibition balance rescues social behavior in *CNTNAP2*-deficient mice. Sci. Transl. Med. *9*, eaah6733.

Thompson, S.M., and Gähwiler, B.H. (1989). Activity-dependent disinhibition. III. Desensitization and GABAB receptor-mediated presynaptic inhibition in the hippocampus in vitro. J. Neurophysiol. *61*, 524–533.

Tomchek, S.D., and Dunn, W. (2007). Sensory processing in children with and without autism: a comparative study using the short sensory profile. Am. J. Occup. Ther. *61*, 190–200.

Treisman, M., and Faulkner, A. (1985). On the choice between choice theory and signal detection theory. Q. J. Exp. Psychol. *37*, 387–405.

Tsukano, H., Horie, M., Ohga, S., Takahashi, K., Kubota, Y., Hishida, R., Takebayashi, H., and Shibuki, K. (2017). Reconsidering tonotopic maps in the auditory cortex and lemniscal auditory thalamus in mice. Front. Neural Circuits *11*, 14.

Turner, D.C., Clark, L., Pomarol-Clotet, E., McKenna, P., Robbins, T.W., and Sahakian, B.J. (2004). Modafinil improves cognition and attentional set shifting in patients with chronic schizophrenia. Neuropsychopharmacology *29*, 1363–1373.

Vaingankar, V., Soto-Sanchez, C., Wang, X., Sommer, F.T., and Hirsch, J.A. (2012). Neurons in the thalamic reticular nucleus are selective for diverse and complex visual features. Front. Integr. Nuerosci. *6*, 118.

Voineagu, I., Wang, X., Johnston, P., Lowe, J.K., Tian, Y., Horvath, S., Mill, J., Cantor, R.M., Blencowe, B.J., and Geschwind, D.H. (2011). Transcriptomic analysis of autistic brain reveals convergent molecular pathology. Nature *474*, 380–384.

Wang, S., Bickford, M.E., Van Horn, S.C., Erisir, A., Godwin, D.W., and Sherman, S.M. (2001). Synaptic targets of thalamic reticular nucleus terminals in the visual thalamus of the cat. J. Comp. Neurol. *440*, 321–341.

Wang, S.M., Han, C., Lee, S.J., Jun, T.Y., Patkar, A.A., Masand, P.S., and Pae, C.U. (2017). Modafinil for the treatment of attention-deficit/hyperactivity disorder: a meta-analysis. J. Psychiatr. Res. *84*, 292–300.

Wells, M.F., Wimmer, R.D., Schmitt, L.I., Feng, G., and Halassa, M.M. (2016). Thalamic reticular impairment underlies attention deficit in Ptchd1(Y/-) mice. Nature *532*, 58–63.

Whitton, J.P., Hancock, K.E., and Polley, D.B. (2014). Immersive audiomotor game play enhances neural and perceptual salience of weak signals in noise. Proc. Natl. Acad. Sci. USA *111*, E2606–E2615.

Wiggins, L.D., Robins, D.L., Bakeman, R., and Adamson, L.B. (2009). Brief report: sensory abnormalities as distinguishing symptoms of autism spectrum disorders in young children. J. Autism Dev. Disord. *39*, 1087–1091.

Wimmer, R.D., Schmitt, L.I., Davidson, T.J., Nakajima, M., Deisseroth, K., and Halassa, M.M. (2015). Thalamic control of sensory selection in divided attention. Nature *526*, 705–709.

Wu, W., and Srivastava, A. (2011). Towards statistical summaries of spike train data. J. Neurosci. Methods *195*, 107–110.

Yang, G.L., and Chen, T.C. (1978). On statistical methods in neuronal spike-train analysis. Math. Biosci. *38*, 1–34.

Yates, J.L., Park, I.M., Katz, L.N., Pillow, J.W., and Huk, A.C. (2017). Functional dissection of signal and noise in MT and LIP during decision-making. Nat. Neurosci. *20*, 1285–1292.

Yu, B.M., Cunningham, J.P., Santhanam, G., Ryu, S.I., Shenoy, K.V., and Sahani, M. (2009). Gaussian-process factor analysis for low-dimensional single-trial analysis of neural population activity. J. Neurophysiol. *102*, 614–635.

STAR★METHODS

KEY RESOURCES TABLE

REAGENT or RESOURCE	SOURCE	IDENTIFIER
Biological Samples		
FuGB2LV-EF1α-DIO-eNpHR3.0-eYFP	Halassa et al., 2014	N/A
AAV2-hsyn-eArch3.0-eYFP	UNC	N/A
AAV2-hsyn-SuperClomeleon	Wimmer et al., 2015	N/A
Chemicals, Peptides, and Recombinant Proteins		
EBIO	Tocris	#1041
Modafinil	Sigma-Aldrich	M6940
Retrobeads IX	LumaFluor Inc	N/A
Experimental Models: Cell Lines		
HEK293FT	ThermoFisher	R70007
Experimental Models: Organisms/Strains		
C57BL/6J	Jackson Labs	#016962
PTCHD1 KO	Wells et al., 2016	MGI:5792693
Ptchd1 $^{y/fl}$	Wells et al., 2016	N/A
Vgat-Cre	Jackson Labs	#000664
SST-Cre	Jackson Labs	#013044
Software and Algorithms		
MATLAB	The MathWorks	https://www.mathworks.com/products/matlab.html
Allen Mouse Brain Connectivity Atlas	Allen Institute	http://connectivity.brain-map.org/projection
Neural Decoding Toolbox	Center for Brains Minds and Machines	http://www.readout.info
Fiji (ImageJ)	NIH	http://fiji.sc

LEAD CONTACT AND MATERIALS AVAILABILITY

This study did not generate unique new reagents. Further information and requests for resources and reagents should be directed to and be fulfilled by the Lead Contact, Michael Halassa (mhalassa@mit.edu).

EXPERIMENTAL MODEL AND SUBJECT DETAILS

Vgat-Cre mice (016962), SST-Cre (013044) and C57BL/6J mice (000664) were obtained from Jackson Laboratory. Global Ptchd1 KO mice were generated as described previously (Wells et al., 2016). TRN specific PTCHD1 KO mice (SST Cre /PTCHD1$^{y/fl}$) were generated by crossing Ptchd1+/fl female mice to SST-Cre mice, which resulted in a loss of this gene that was essentially limited to the TRN, as shown in a previous study (Wells et al., 2016). All global and specific KO lines as well as Vgat-Cre mice used in this study were backcrossed to C57BL/6J mice for at least 6 generations to obtain a homogeneous genetic background. All mice tested were between 2-14 months of age and housed on a 12-h light/dark cycle. Male mice were used for behavioral testing to reduce potential confounds from placing mice both genders sequentially in the same behavioral testing environment, while mice of both sexes were used for all other experiments. Throughout these experiments, all procedures were performed in accordance with protocols approved by the Institutional Animal Care and Use Committee at the New York University Langone Medical Center and by the Committee on Animal Care at the Massachusetts Institute of Technology. All procedures are also in accordance with guidelines issued by the US National Institutes of Health.

METHOD DETAILS

Behavioral Training and Testing

Testing/Training Setups for Behavioral Task

Behavioral training and testing took place in grid-floor mounted, custom-built enclosures made of acrylic plastic (maximum dimensions in cm: length: 15.2; width: 12.7; height: 24). All enclosures contained custom-designed operant ports, each of which was equipped with an IR LED/IR phototransistor pair (Digikey, Thief River Falls, MN) for nose-poke detection. Trial initiation was achieved through an initiation port mounted on the grid floor ~6 cm away from the 'response ports' and 'reward ports' located at the front of the chamber. Response and reward ports were stacked with the response port on top. Access to all response and reward ports was restricted by vertical sliding gates which were moved via a rack and pinion gear system powered by a servo motor (Tower Hobbies, Champaign, IL). Reward ports were capable of delivering a milk reward (volume > / = 4 μL evaporated milk, delivered via a single-syringe pump (New Era Pump Systems, Farmingdale, NY)) when a correct GO or NO GO response was made.

A pair of electrostatic speakers (Tucker Davis Technologies, Alachua, FL) producing the auditory stimuli were placed outside of the training apparatus and sound stimuli were conveyed via cylindrical tubes to apertures located at either side of the initiation port, allowing consistent delivery of stereotypical stimuli across trials. All stimuli and auditory cues across tasks were generated by a TDT Rx8 sound system (Tucker-Davis Technologies, Alachua, FL). Sound stimuli and auditory cues were recorded and assessed for frequency content and intensity using a prepolarized icp array microphone (PCB Piezotronics, Depew, NY) after which frequency production was equalized using software-based calibration via SigCalRP (Tucker-Davis Technologies, Alachua FL).

Trial availability was indicated by illumination of a dimmable, white-light-emitting diode (Mouser, El Cajon, CA) mounted on the top front of the enclosure and controlled by an Arduino Mega microcontroller (Ivrea, Ital). Noise cues for noisy auditory discrimination task (see below) were produced by UV (320-380nm) or Green (495-510nm) light emitting diodes (Mouser, El Cajon, CA) mounted on the top of the enclosure and controlled by Arduino Mega microcontroller (Ivrea, Italy). The TDT Rx8 system (Tucker Davis Technologies, Alachua, FL) was used to produce sounds within the mouse hearing range. Sound presentation was controlled through MATLAB (MathWorks, Natick, MA), interfacing with a custom written software running on an Arduino Mega (Ivrea, Italy) for trial logic control.

Training and Testing

Mice were food restricted to 85%–90% of their *ad libitum* body weight before training. A total of 14 control and 20 Global KO and 4 TRN specific KO mice were trained on this task. No differences were observed in learning between these groups. Animals were first trained to initiate trials after which they were trained to perform the basic discrimination task (~3 weeks daily training). In training and testing, mice initiated each trial by holding their snout in an initiation port for at least 50 ms to initiate a delay period 500 ms. Following a 500 ms delay, a pure tone stimulus was played for 100ms from speakers on both sides of the initiation port at an intensity of 60 dB. Animals were trained to hold their head in the initiation port throughout the delay and stimulus delivery. One of three pure tone stimuli were then played. A 20 kHz tone signaled a target, "GO" response, while two frequencies above or below 20 kHz (16 or 24 kHz) signaled a non-target "NO GO" response. The pure tone stimuli were pseudo-randomly varied on a trial by trial basis, with trials divided between the "GO" stimulus (~40% of trials) and two "NO GO" stimuli (16 and 24 kHz, ~30% of trials per frequency). The order of "NO GO" stimuli followed a pre-determined pseudorandomized sequence. After stimulus presentation, the response port was made accessible for a 2.5sec trial period. In "GO" trials, the mouse was required to poke in this response port within the trial period (a "Hit") in which case a reward port directly underneath the response port became accessible and reward was delivered. For a "Miss" in which the mouse failed to poke within the trial period, the reward port was not made accessible. For a "correct rejection," withholding for the full 2.5sec when the "NO GO" stimulus was played, the reward port was made accessible. For a "False Alarm" response on a "NO GO" trial, the reward port was not made accessible. For both types of incorrect response (False Alarm and Miss) animals were punished with delay in the availability of the next trial by an additional 15 s time-out period. To increase task engagement and reduce the tendency to guess on a subset of trials, reward volume was increased in proportion to the number of consecutive correct responses with 2 μL of evaporated milk added for every two consecutive correct trials.

To parametrically vary stimulus signal to noise ratios (SNR), white noise was added to pure tone stimuli at fixed stimulus SNR ratios as labeled in each relevant figure. The SNR values correspond to addition of white noise using the awgn function in MATLAB with a constant 60dB maximum intensity of the signal tone (SNR_{input}). To obtain the effective SNR more typically used in auditory research ($SNR_{observed}$), the RMS of the tone and noise were calculated for recorded stimuli. For the SNR_{input} values used ([0.6 1.0 1.8 2.4 3.2 5.6 10]) the calculated $SNR_{observed}$ values were ([-10.7 −1.4 0.6 2.0 4.0 10.5 21.1] dB). These values fall in the range typically associated with difficult levels of auditory masking in mouse behavioral tasks (Whitton et al., 2014).

In the basic discrimination task, 60% of total trials were randomly masked by noise (average session length = 212 trials). Following initial introduction of noise, performance on noise trials dropped precipitously in control and KO mice even for low noise levels. For the lowest noise levels, however, performance recovered close to baseline levels in control and KO, and a similar, but partial recovery was observed for high noise conditions as well. Because of this, mice were trained for an additional 1-2 weeks following noise introduction with a mixture of noise intensities prior to testing. For the cued noisy auditory discrimination, a Green (495-510 nm) or UV (320-380 nm) light was activated for 100 ms following the start of initiation. Through multiple sessions prior to testing (~2 months daily training following initial task acquisition) mice were trained to expect a noise trial following one of the two light colors on 100% of trials (predictive cue) and a 50% chance of noise following the other color (unpredictive cue). Mice were divided into two equal groups with the predictive cue assigned to UV in one group and green in the other. Groups were of equal size for each

experiment with a minimum of 2 mice in each. After the light cue, or a 100 ms cue free period for uncued trials, animals were required to hold through an additional 400 ms delay period prior to the sound stimulus playing.

During testing in the cued noisy auditory discrimination task, trials were divided into subsets for different noise/cue combinations. In each session, ~40% of total trials were pure tone without noise (SNR = 120) and were either uncued or cued with the unpredictive cue (uncued 25% total, unpredictive cue 15% total). The remaining 60% of total trials were noise trials (SNR 0.5-10) divided among all three cueing conditions (predictive cue 30% total, unpredictive cue 15% total, uncued 15% total). Each session included only one SNR level for the noise trials. After this second training stage, mice were injected with viral vectors and implanted with optic fibers or microdrive (see relevant sections below). Following recovery, each animal was re-trained to a performance level of > 70% in pure tone trials (SNR = 120). Only sessions with the performance above 70% in pure tone trials (SNR = 120) were used for analysis.

Behavioral Analysis

Performance on the discrimination task was initially assessed using the d' statistic (d' = Z(hit rate) – Z(false alarm rate)). For all experiments, sessions were only included if baseline performance was ≥ 65% correct (SNR = 120). Noise-masking behavior with multiple SNR levels was averaged across sessions (d' was calculated for each session and noise-level, then averaged) and fit with a logistic function. For predictive cue behavioral experiments, these trial types were initially grouped within sessions and d' values were calculated on a session by session basis. Only sessions in which at least 25 trials of a given type occurred were included. For comparisons at multiple SNR levels, performance on each trial type was pooled within sessions for each SNR level (one SNR level was included per session) and d' was calculated. To estimate parameters of psychometric functions across noise levels, d' averages for all SNR levels were fit with the logistic function:

$$F(x;\alpha,\beta,\lambda) = \frac{(\lambda)}{1+exp(-\beta(x-\alpha))}$$

where x corresponds to the inverse of the ratio between the intensity of added noise and the maximum sound intensity of the stimulus (i.e., stimulus SNR) in log-scale, α corresponds to the detection threshold and λ corresponds to the maximum performance associated with behavioral "lapse rate" (Wimmer et al., 2015). Fitting was made using the Palamedes psychophysical toolbox (http://www.palamedestoolbox.org/) via maximum likelihood estimation. Confidence interval estimates were then made using a bootstrapping procedure in which subsets of sessions were selected at random across mice (60% selection per subset per SNR level) with parameters estimated by fitting the resulting data for each subset.

To estimate the performance benefit provided by a noise predictive (or unpredictive) cue, the performance (d') for individual SNR levels in uncued trials within each session was subtracted from the corresponding performance on cued trials. The resulting function, being a change between logistic cumulative distribution functions, was then fit using the logistic probability density function (Treisman and Faulkner, 1985):

$$F(x;\alpha,\beta,\lambda) = \frac{exp^{-\beta(x-\alpha)}}{(1+exp(-\beta(x-\alpha)))^2/\beta}$$

The parameters of this function correspond to parameters in the original function used to fit the raw data, as described above.

To compare performance of control and KO as well as performance in KO mice treated with EBIO, modafinil, and the combination of the two, discrimination thresholds were compared in a pairwise fashion across these various conditions using rank-sum comparisons of the bootstrap estimates for these parameters. To correct for multiple comparisons, the Bonferroni correction (division of the threshold p value corresponding to 0.05, 0.01 or 0.001 by the number of comparisons made) was used for pairwise testing with the correction made across individual traces as well as change in discrimination threshold. All comparisons were included in the correction (16 comparisons in total).

Optical Chloride Measurements in Behavior

For combined TRN optical recordings with/without optogenetic PFC disruption, laser trains of yellow light were delivered during the initiation period on a random subset of trials as described above. The FRET-based measurement of sound-evoked $[Cl^-]_I$ responses was performed as previously described (Wells et al., 2016; Wimmer et al., 2015) with some methodological improvements to enhance signal level, as described below. For these recordings, excitation of SuperClomeleon CFP and YFP along with their emitted light were carried through chronically implanted optical fibers using a specialized, custom constructed triple fiber (total inner diameter 660 μm, Doric lenses) which was connected with a 400μm, 0.48NA optic patch cord to the recording system. This triple fiber consisted of three angled mirror fibers (60 degrees, NA 0.66) which surrounded the sampled structure. These fibers were oriented toward the sampled structure allowing them to both provided CFP excitation (430 nm light) and collect emissions within the optimally excited zone. The three fibers were collimated through a custom lens system to connect to a common patch cord through which excitation light was also delivered. Recordings were made using the Assisted Rotating Fluorescence Mini Cube (ARFMC) for FRET system (Doric lenses, Quebec, Canada). Although minimal artifacts were observed, to reduce laser-light artifacts, optogenetic manipulations were delivered via angled optical fibers oriented away from the recording fibers.

Virus Set and Injection Coordinates

All AAVs were produced by either the vector core at the University of North Carolina Chapel Hill viral core with titers above 10^{12} VG/ml. All FuGB2LV were produced in our laboratory with titers above 10^{8} VG/ml. FuGB2LV was produced as described previously (Halassa et al., 2014). The expression plasmid and two helper plasmids, delta8.9 and FuGB2 (Kato et al., 2011), were transfected into human embryonic kidney 293FT cells with Polyethylenimine "Max" (PEI; Polyscience, Inc; 24765). Viral particles were collected from the cell culture medium, pelleted by ultracentrifugation at 50,000 x g(m/s^2) for 2 h. Coordinates for each injection were as follows (in mm, A/P, M/L from Bregma, D/V from brain surface): MGBv: A/P: −3.2 mm, M/L: ± 2.0 mm, D/V: −3.0 mm; PFC: A/P: 2.4 mm, M/L: ± 0.6 mm, D/V: −1.4 mm, MD: A/P: −1.34 mm, M/L: ± 0.6 mm, D/V: −2.8 mm. Mice were anesthetized using 1% isoflurane and mounted on a stereotactic frame for virus injections. For behavioral experiments, mice were allowed to recover for 2-4 weeks following virus injection to allow expression prior to testing.

Optogenetic Experiments

For audTRN optotagging, audTRN neurons were labeled through injections (0.4-0.6 μl) of FuGB2LV-EF1α-DIO-eNpHR3.0-eYFP in MGBv of Vgat-Cre mice. For optogenetic PFC or MD suppression during behavior, 0.4 μL of AAV2-hsyn-eArch3.0-EYFP was injected into PFC or MD.

Optic fiber Implantation

As with viral injections, mice were anesthetized using 1% isoflurane and mounted on a stereotactic frame. For optogenetic experiments, up to four pairs of 200 μm optic fibers (Doric Lenses, Quebec, Canada) were stereotactically inserted at the following coordinates (in mm A/P, M/L from Bregma, D/V from brain surface): PFC: A/P: 2.6, M/L: ± 0.6, D/V: −1.0; audTRN: A/P: −1.8, M/L: ± 2.3, D/V: −2.8. MD: A/P: −1.34, M/L: ± 0.6, D/V: −2.5.

For fiber photometry experiments, custom constructed triple fibers were implanted bilaterally in the MGBv (A/P: −3.2, M/L: ± 1.8). To optimize signal quality in these experiments, fibers were implanted into pre-injected mice two weeks after virus injection. During implantation, fluorescence measurements were made continuously while fibers were slowly advanced toward the target. During this targeting, broadband sounds were delivered to the contralateral ear at regular intervals. Once sound-related events were observed in the optical signal, the depth was recorded and fibers were fixed in place using dental cement.

In combined optogenetic and fiber-photometry experiments, 45° angled optical fibers were implanted posterior to the PFC (A/P: 2.6, M/L: ± 0.6, D/V: −1.0) and oriented toward the anterior to minimize light contamination in the optical recordings. Up to 3 stainless-steel screws were used to anchor the implant to the skull and everything was bonded together with dental cement. Mice were allowed to recover with *ad libitum* access to food and water for one week after which they were brought back to food regulation and behavioral training resumed.

Microdrive Array Construction and Implantation

Custom drive housings were designed using 3D CAD software (SolidWorks, Concord, MA) and printed in Accura 55 plastic (American Precision Prototyping, Tulsa, OK) as described previously (Liang et al., 2017). Prior to implantation, each drive was loaded with 12-24 independently movable microdrives carrying 12.5μm Stablohm 650 (California Fine Wire Company, Grove Beach, CA) tetrodes. Electrodes were pinned to custom-designed 96- or 128-channel electrode interface boards (EIB, Sunstone Circuits, Mulino, OR) along with a common reference wire (A-M systems, Carlsborg, WA). For combined optogenetic tagging and electrophysiological recordings of audTRN, mirror-tipped optical fibers delivering the light beam at right angles (MFC_200/245-0.37_34mm_MF1.25_MA45, Doric Lenses, Quebec, Canada) were embedded in our implants anterior to the electrode arrays and oriented posteriorly toward the audTRN. For high-density bilateral recordings of MGBv, we constructed drives with static, non-movable electrodes (implantation targeting is described below for these drives).

For combined optogenetic manipulations and electrophysiological recordings of the PFC, optic fibers delivering the light beam lateral (MFC_200/245-0.37_34mm_MF1.25_MA45, Doric Lenses, Quebec, Canada) were embedded adjacent to the electrodes. For combined optogenetic manipulations of the contralateral PFC or ipsilateral MD with PFC recordings, the optical fiber was incorporated adjacent to the electrode array at the appropriate spatial offset.

During drive implantation, mice were deeply anesthetized with 1% isofluorane and mounted on a stereotaxic frame. Burr holes were drilled for optical fibers when necessary. A craniotomy was drilled centered at A/P 2 mm, M/L 0.6 mm for PFC recordings (~1 × 2.5 mm), at A/P −1.8 mm, M/L 2.0 mm for audTRN recordings (~2 × 2 mm), at A/P −1mm, ML 1.2mm for MD recordings(~2 × 2 mm), or at A/P −3.2 mm, M/L 2.0 mm for MGBv recordings (~2 × 2 mm). The dura was carefully removed and the drive implant was lowered into the craniotomy using a stereotaxic arm until electrode tips touched the cortical surface. Surgilube (Savage Laboratories, Melville, NY) was applied around electrodes to guard against fixation by dental cement. Stainless steel screws were implanted into the skull to provide electrical ground and mechanical stability for drives and the whole construct was bonded together and attached to the skull using C&B-Metabond luting cement (Parkell, Edgewood NY). For head-fixation experiments, a custom-designed 3D-printed hexagonal plastic crown (MakerBot Replicator, Brooklyn NY) was implanted encircling the drive at its base.

In the subset of surgeries that used static implants for MGBv recordings, online targeting was necessary to ensure accurate electrode placement. In these cases, the drive was connected to our data-acquisition system for electrophysiological recordings (see below, Electrophysiological Recordings) when being lowered into the brain. Once the drive was lowered to within 500 μm of the target

depth, we presented bilateral auditory stimuli (dynamic random chords presented with EC1 electrostatic speakers with an ED1 speaker driver, Tucker Davis Technologies, Alachua FL). The drive was then advanced in steps of 100 μm until we observed auditory-responsive units. The drive was then advanced an additional 250 μm to target the ventral MGB. If auditory responsive units were still observed, the drive was and then bonded to the skull as described above. Otherwise, the drive was raised with 50 μm steps until sound responsive units were observed.

Head Fixation and Stimulus Delivery System

Recordings of MGBv and audTRN sensory responses were conducted in a custom head-fixation/sound-delivery system enclosed in a ventilated sound-proof chamber (IAC Acoustics, North Aurora, IL). The head-fixation system consisted of a pair of custom 3D printed plastic fixation clamps (MakerBot Replicator, Brooklyn NY) used to lock the implanted plastic crown at the base of the implant into place during recordings (see Figure 1D for illustration). These were fixed to an acrylic plastic frame which also supported a platform on which the animal stood. The platform was composed of low-friction acrylic and was adjusted based on the height of the animal and spring-loaded to minimize torque on the implant. For head fixed recordings, stimuli were delivered from a pair of electrostatic speakers on either side of the animal via straight, plastic tubes 2 cm long which terminated 2.5 mm from each ear.

Electrophysiological Recordings

Signals from tetrodes were acquired using a Neuralynx multiplexing digital recording system (Neuralynx, Bozeman MT) via a combination of 32- and 64-channel digital multiplexing headstages plugged to the 96- or 128-channel EIB of each implant. Signals from each electrode were amplified, filtered between 0.1 Hz and 9 kHz and digitized at 30 kHz. For audTRN recordings, tetrodes were lowered over the course of 1-2 weeks from the cortex into the target structure. For PFC recordings, adjustments were more targeted, consistent with the more superficial position of the region of interest. The system used for recordings (head fixed and in-behavior) was entirely automated so no investigator blinding of genotype or drug conditions was required for electrophysiological experiments. Following acquisition, spike sorting was performed offline based on relative spike amplitude and energy within electrode pairs automatically using MountainSort as previously described (Chung et al., 2017; Nakajima et al., 2019; Rikhye et al., 2018a). After initial clustering, units were divided into fast spiking (FS) and regular spiking (RS) based on waveform characteristics as previously described (Halassa et al., 2014). Briefly, peak to trough time was measured in all spike waveforms, and showed a distinct bimodal distribution (Hartigan's dip test, $p < 10^{-5}$). These distributions separated at 178 μs, and cells with peak to trough times above this threshold were considered RS while those with peak to trough times below were considered FS cells. This initial identification was subsequently further validated in two feature dimensions (Half Trough time versus Peak to Trough time) using k-means clustering which showed good agreement with the single dimension separation (97% overlap in cell selection). In the MGBv, we recorded a total of 854 RS neurons from 6 control mice as well as 711 RS neurons in 3 KO mice. In the audTRN, we recorded a total of 602 FS neurons from 3 control mice as well as 636 FS neurons in 3 KO mice. In the PFC, we recorded a total of 2304 RS neurons and 408 FS neurons from 8 control mice as well as 1742 RS neurons and 345 FS neurons in 4 KO mice.

MGBv and audTRN Specific Methods

In MGBv and audTRN recordings, neurons were considered sound responsive if their firing rate was significantly elevated across at least 20 percent of the stimulus period (8x25 ms bins). For somatic recordings, MGBv projecting TRN neurons (audTRN) were identified using retrograde optogenetic tagging resulting in expression of eNpHR 3.0. Neurons were considered tagged if their firing rate showed a significant decrease in firing rate within 25 ms of laser pulse onset. Significance testing was based on estimation of the 95% confidence intervals for peri-stimulus time histograms (PSTHs) generated from 100 sound stimuli or laser pulses as previously described (Wimmer et al., 2015).

For firing rate, as well as Fano factor quantification, stimuli consisted of 20 dynamic random chord (DRC) sound stimuli repeated 20 times each. To record responses to noisy sound stimuli, same number of DRC stimuli were repeated 20 times each with added broadband noise (SNR 3.2). As with the pure tone stimuli used in behavior, the DRC signal to noise ratios (SNR) was parametrically varied by adding Gaussian white noise at fixed stimulus SNR ratios using the awgn function in MATLAB with a constant 60dB maximum intensity of the highest intensity DRC tone stack (SNR_{input}). To obtain the effective SNR more typically used in auditory research ($SNR_{observed}$), the RMS of the tone and noise were calculated for recorded stimuli. For the SNR_{input} values used ([0.6 1.0 1.8 2.4 3.2 5.6 10]) the calculated $SNR_{observed}$ values were ([-10.7 −1.4 0.6 2.0 4.0 10.5 21.1] dB) for single tones within the DRCs. These values fall in the range typically associated with difficult levels of auditory masking in mouse behavioral tasks (Whitton et al., 2014). Firing rates for the evoked responses were then obtained during stimulus (DRC or DRC + noise) presentation.

In additional sets of experiments, we sought to assess responses of audTRN to increasing intensities of broadband noise without embedded DRCs. Noise pulses were delivered in one second pules. The intensities measured in the sound-proof chamber took the following values (in dB): [7(no added noise) 23 30 41 57 80 114]. Responses of audTRN were fit using a with the Weibull function:

$$W(x) = r_{max} * \left(1 - e^{-\left(x_{/\alpha}\right)^{\beta}}\right)$$

Where r_{max}, α, and β are fitted parameters. The first two (r_{max} and α) correspond to the maximum firing rate and the half-maximal input value respectively. Similar values were obtained by fitting with a logistic function.

Connectivity Assay

To assess the impact of changes in MD excitability on cortical connection strength, we measured intra-cortical responses evoked by ChR2-mediated activation of the contralateral PFC with and without suppression of the MD. Responses to either cortical stimulation alone (0.01 s ChR2 activation to the contralateral PFC), thalamic suppression alone (0.25 s eNpHR3.0 activation) or both (the same 0.25 s eNpHR3.0 activation beginning 0.1 s before the same ChR2 activation pulse) were recorded in PFC (100 interleaved trials per condition).

Fano Factor

Fano factor values were computed for each MGBv neuron based on their responses across 20 repeated deliveries of each DRC stimulus. This computation was made using MATLAB code which is included in the variance toolbox (available online at https://churchland.zuckermaninstitute.columbia.edu/content/code) as described previously (Churchland et al., 2010). Briefly, spike counts were computed in 12.5 ms windows aligned to the chords of the DRC for each trial. Spike count means and variance were then computed across trials. The mean and variance across DRC stimulus chords were compiled and fitted with a regression line. The slope of this line was taken as the Fano factor for this cell. This "raw" Fano factor (Churchland et al., 2010) was used across neurons and conditions for comparisons. To estimate the noise effect on response precision, Fano factor was first computed for the non-noise and noise conditions separately for each cell after which values for the noise condition were subtracted from the non-noise.

Identification of peaks in task-modulated neurons

In assessing delay period responses in the cued noisy discrimination task, we rarely observed individual PFC neurons that exhibited sustained increases in spiking relative to baseline (consistent with previous results both in this task (Nakajima et al., 2019) and in related attentional tasks (Schmitt et al., 2017)). However, a subset of cells showed a brief elevation (peak) of spiking activity at a defined moment in the delay period. Across both tasks, these neurons were identified based on consistency in their spike timing across correct trials, as well as cross-trial elevation in spike rate as follows:

First, periods of increased consistency in spike-timing across trials were identified using a Matching-Minimization algorithm (Wu and Srivastava, 2011). This was used to determine the best moments of spike time alignment across trials (putative peak times). These putative peak times were obtained as the solution of the equation:

$$S = \arg_{C \in S} \min \sum_{k=1}^{N} d_2(S_k, C)^2$$

In which the putative peak times across trains (S) was obtained by minimizing the sum of the distance function (d_2) of the observed spike trains (S_k) and the current peak time estimate (C) given a set of penalty coefficients associated with spike time translation. Initially, spikes in C were placed arbitrarily within the sample window. The number of spikes (n) included in the initial estimate was obtained by minimizing the equation:

$$\sum_{k=1}^{N} |n_k - n|$$

Where n_k is the number of spikes in a trial and n is the number of putative peak locations. Thus, the initial number of putative peaks is equal to the median number of spikes observed within the sample period across spike trains. From this starting condition, putative peak times were iteratively adjusted to minimize the distance function (d_2) between the observed spikes and the putative peak-time estimate. This adjustment was based on the relative ISI values of the peak time estimate (f) and the spike train for each trial (g) based on the equation:

$$d_p(f,g) = \left(\lambda \sum_{k=1}^{M+1} \left| (\Delta gs_k)^{\frac{1}{p}} - (\Delta fs_k)^{\frac{1}{p}} \right|^p \right)^p$$

Where Δgs_k and Δfs_k are vectors of the interspike intervals associated with the peak time estimate and the spike train of a given trial, respectively, M is equal to the total number of spikes, λ is the cost penalty weight and p is the comparison parameter (in this case 2 for pairwise comparisons). If the distance for a given putative peak in the estimate was optimal (e.g., the distance is at the local minimum) then it was left in place, otherwise it was moved via linear interpolation between its current location and the measured spike times across trials, placing it in the center of the interpolation line. Finally, the overall distance was minimized by adjusting the interspike interval using the spike ISI average metric, a solution to the minimization equation (above). The putative peak times were updated using the newly calculated ISIs after which the variance was computed. These steps were iterated until the variance converged. The resulting spike times were taken as putative peak locations.

To determine whether a peak occurs at any of these putative locations, we applied two further criteria. First, for 75% of the trials, at least one spike must fall within ± 25 ms of the putative peak time. This conservative threshold was based on the median firing rates observed during the task period which in the majority of cells is less than 10 Hz predicting that the most spike intervals between trials will be greater than 50 ms (1/2 peak ISI for this firing rate). Second, we incorporated a z-score criterion which is sensitive to changes in

the number of spikes occurring in a particular time-bin across trials. The z-score was computed relative to the pre-delay baseline (10 ms binning, convolved with a 25 ms half-width Gaussian kernel). If the z-score within the 50 ms window surrounding the potential peak exceeded 1.5 for a cell meeting the first criterion, then this time point was considered a true peak and the cell identified as a task-modulated unit.

Decoding Analysis

To assess tone representation in the MGBv and predictive/unpredictive cue representations in the PFC we applied a population decoding approaches, the Poisson Naive Bayes (PNB) classifier, as implemented in the neural decoding toolbox (Meyers, 2013). This analysis was applied to sound responsive MGBv neurons as well as to all neurons in the PFC recorded during behavior. In each case, neurons recorded from either structure each of which were pooled into a pseudo-population for each subset of cells within a condition. For classification, neuron spiking activity was modeled as a Poisson random variable with each neuron's activity assumed to be independent. The model was based on spike counts of these pseudo-populations (Meyers, 2013). Analysis was performed based either on spiking associated with stimulus (MGBv) or cue type (PFC) as described below.

MGBv Decoding

To effectively assess the encoding of sounds relevant to behavior, we decoded the activity of neural populations recorded in the MGBv that represents sounds used in behavior. We focused on decoding pure tones with frequencies of 20 kHz and 24 kHz, the more difficult discrimination. To quantify the effect of noise, we assessed the response to these pure tones with added noise. Spike trains were taken from MGBv responses elicited either by tones presented alone (SNR = 120) or with different levels of masking noise (SNR = 3.2, or 1.8). Stimuli (25 ms duration) were presented at 100 ms intervals (100 repetitions per noise condition). Spike trains of MGBv responses used for decoding began 25 ms before the stimulus onset and terminated 50 ms after (75 ms total).

To train the classifier, spike trains were repeatedly and randomly subsampled (60 resampling runs) and divided into training and test subsets (10 trials sampled 6 used for training and 4 for testing). For each subsampling, the classifier was trained using the training subset to produce a predictive mean response template $(\bar{x})$ for each stimulus tone (i). Templates were constructed separately for 25 ms time bins across the trace (step size = 25 ms) and with the classifier trained for each template. In the cross-validation step, these templates were used to predict the class for each test trial in the test set (x^*) by maximizing the log likelihood decision function $([i^* = \mathit{arg}\max_i \mathrm{LL}(x^*, \bar{x})])$ as described previously (Duda et al., 2001). The overall likelihood value can then be calculated by multiplying the probabilities for each neuron together (under the assumption that each neuron is independent). The prediction accuracy (decision values) were quantified as normalized rank in the posterior probability list (Meyers, 2013; Mitchell et al., 2004). We used the maximum prediction accuracy within the three time bins after tone onset. This allowed us to look at activity elicited by the tone at various offsets during which it is physiologically plausible that the tone is encoded in the MGBv (Anderson et al., 2009). To determine the variability of this estimate, a bootstrapping procedure was applied in which 60% of neurons were subsampled from the overall population and the same procedure was repeated (50 resampling runs) and the maximum prediction accuracy was estimated for these subsamples. These decoding accuracy values were grouped across time points / subsamples for each condition and used for comparisons.

PFC Decoding for cued noisy auditory discrimination

Spike trains, which included spiking 1 s before and 1.5 s after initiation, from correct trials were first divided into those in which animals were cued with a predictive cue, those in which an unpredictive cue was presented and those in which no cue was presented. For most comparisons, decoding was performed comparing trials in which the predictive cue was delivered with those in which the unpredictive cue was delivered. Neurons from mice trained with different meaningful cue types were combined in a single group. This approach was designed to reduce the chance that stimulus related activity, rather than the rule meaning, was primarily responsible for the information decoded from the population.

To train the classifier, spike trains were repeatedly and randomly subsampled (60 resampling runs) and divided into training and test subsets (10 trials sampled 6 used for training and 4 for testing). The classifier was trained on these subsets to produce a predictive mean response template $(\bar{x})$ for each trial type (i). Templates were constructed separately for 50 ms overlapping windows across the trace (step size = 25 ms) and with the classifier trained for each template allowing a temporal profile to be estimated. In the cross-validation step, these templates were used to predict the class for each test trial in the test set (x^*) by maximizing the log likelihood decision function $([i^* = \mathit{arg}\max_i \mathrm{LL}(x^*, \bar{x})])$ as described previously (Duda et al., 2001). The overall likelihood value can then be calculated by multiplying the probabilities for each neuron together (under the assumption that each feature is independent). The prediction accuracy (decision values) were quantified as normalized rank in the posterior probability list (Meyers, 2013; Mitchell et al., 2004). To determine the variability of this estimate, a bootstrapping procedure was applied in which 60% of neurons were subsampled from the overall population and the same procedure was repeated (50 resampling runs). The resulting traces were used to estimate the 95% confidence intervals of the initial estimate from the full population. For group comparisons, prediction accuracy was estimated based on the activity of these subsamples at each time point during the delay period and the decoding accuracy was grouped across time points/subsamples. To assess the encoding of task relevant information in KO and control mice, we used an approach intended to match the number of neurons included while also ensuring that neurons included showed task relevant activity. More specifically, for these comparisons neurons recorded across control or KO mice during task performance were sorted based on their maximum change in spiking rate during delay periods in which either a predictive or unpredictive cue was delivered, normalized relative to baseline rates. Only the top 100 neurons were used for analysis.

Generalized Linear Model Based Coupling Estimation

To assess interactions among simultaneously recorded neurons in the PFC, we modeled spike trains of these cells using a generalized linear model (Park et al., 2014; Pillow et al., 2008; Yates et al., 2017) as we have done previously (Rikhye et al., 2018a). For this analysis, spike trains were discretized into 1 ms bins. As described previously (Pillow et al., 2005) the log-likelihood for the activity of a single neuron was taken as:

$$\log L(\varphi, r) = \sum_{t} r(t) \log(\Delta\varphi(t)) - \Delta\varphi(t)$$

With $\varphi(t)$ being the instantaneous spiking rate (conditional intensity) arising from the fully coupled GLM based on the input parameters being estimated. This relationship is described by the following equation:

$$\varphi(t) = \exp(\boldsymbol{k} * x(t) + \boldsymbol{h} * r(t-1) + \boldsymbol{c} * s(t-1) + b)$$

Where the vector $\boldsymbol{k}$ is the estimate of the weights associated with the stimulus covariates (similar to a sensory receptive field); $\boldsymbol{h}$ is the estimate of the weights which quantify the influence of the neuron's own spiking history on the current activity; $\boldsymbol{c}$ corresponds to the weights quantifying the strength of interactions (coupling filters) based on the spiking activity $(s(t-1))$ of other simultaneously recorded neurons in earlier time-bins. To limit the possibility of overfitting, regression weights were fit with a *maximum a posteriori* estimate that included an L2 penalty. This fitting method is based on a previously applied approach (Park et al., 2014). The source code for scripts used are available to be downloaded (https://github.com/pillowlab/neuroGLM).

The coupling filters estimated using this method are essentially analogous to the positive lag portion of a cross-correlogram after response various explained by the cue, other task-relevant variables and the interactions with other neurons is taken into account. For a given neuron, then, a coupling filter is estimated that explains part of the variance in the activity of the neuron being modeled when convolved with the spike train of the modeled neuron. This operation can be expressed mathematically as:

$$\sum_{i=1}^{m} \sum_{j=1}^{n} c_{ij} f_i(s_i(t-\tau : t))$$

Where i indexes the number of neurons recorded simultaneously (m) and j indexes the temporal basis functions f_i for spiking of these neurons across time with c_{ij} being the relevant coupling filter. We assumed the temporal basis functions to be nonlinearly time-scaled raised cosine functions base on previous methods (Park et al., 2014). For each session, the GLM was constructed using a median of 61 simultaneously recorded PFC neurons with well isolated units.

Estimation of coupling filters used spiking of the included neurons over the delay period for each cue condition separately as well as spike prior to initiation (−500 ms to initiation). Coupling filters estimated with from this data were statistically validated using leave-one-out cross validation (Yu et al., 2009). All coupling filters from putative excitatory (RS) neurons were included for subsequent analysis. The functional coupling among the network was quantified by taking the area under the curve for the positive going components of these estimated filters (which can be taken as a measure of excitatory connectivity) for all modeled neurons. These values were accumulated across sessions for both control and KO mice.

Pharmacological Manipulations

All drugs used in this study for either behavioral or electrophysiological experiments were purified to > 98% (HPLC). Based on previous assessment of the optimal time-course and mode of administration for EBIO to influence thalamic inhibition in the KO (Wells et al., 2016), EBIO (Tocris #1041; 25 mg/kg in 25% DMSO/saline; subcutaneous injection), or vehicle was administered 30 mins prior to behavioral testing. In preliminary experiments, a similar time-course was observed for the effect of modafinil (Sigma# M6940; 13mg/kg in 25% DMSO/saline; intra-peritoneal injection). Based on these preliminary assessments, for behavioral experiments injections of drug or vehicle solution were made 30 min prior to testing. To determine the effect of each of these pharmacological manipulations on thalamic or cortical unit activity, first recordings were made from the relevant structure for 1-2.5 h following vehicle injection. Then drug (modafinil or EBIO) was injected and recordings were continued for an additional 1-2.5 h. For PFC recording during behaviors, after 150 trials following vehicle administration, mice were injected with drug and kept outside of the behavior box. After 30 mins, mice were placed back into the behavioral box and run for another block of 150 trials. Drug effects were determined based on recordings of activity in the second behavior block.

Slice Recordings

Identification and recording of audTRN neurons

For identification of audTRN neurons, mice (3-4 weeks old) were injected 48 h before an experiment with 150 nL of either red or green Retrobeads IX (*LumaFluor*, 1:10 dilution in 0.9% saline) to MGB at the following stereotaxic coordinates: −3.10 mm AP, −2.05 mm ML, −3.10 mm DV. AP and DV measures were scaled proportionally to the distance between Lambda and Bregma. For tissue collection, artificial CSF (aCSF) was prepared fresh daily at 310 mOsm containing in mM: 125 NaCl, 25 $NaHCO_3$, 2.5 KCl, 1.25 NaH_2PO_4,1.2 $MgCl_2$, 2 $CaCl_2$, 25 glucose, 1.7 L(+)-ascorbic acid, pH 7.4 and saturated with 95% O_2/5% CO_2. Additionally, a protective cutting solution was prepared which exchanged half of the NaCl with sucrose. Following induction of anesthesia with

isoflurane, the brain was removed, and acute horizontal 300 um slices were collected in ice cold cutting solution on a Leica VT1000S vibratome. Slices were then incubated in normal aCSF (containing in mM: 125 NaCl, 25 $NaHCO_3$, 2.5 KCl, 1.25 NaH_2PO_4,1.2 $MgCl_2$, 2 $CaCl_2$, 25 glucose, 1.7 L(+)-ascorbic acid, 310 mOsm) for 45 min at 34°C in a Brain Slice Keeper (*Scientific Systems Design*) and kept at room temperature thereafter. Slices were then placed in a recording chamber which was continuously superfused with oxygenated aCSF and warmed to near-physiological temperature (30–32°C) with a PM-1 heated platform and a TC-3443C temperature controller (*Warner Instruments*). Tissue was visualized on an Ultima Multiphoton Microscope System (*Bruker*) with a Guppy Pro camera (*Allied Vision*), and labeled audTRN neurons were identified using an X-Cite 120 Q fluorescence illuminator. Micropipettes (3.5 – 5.5 MOhms) were prepared with a Sutter P-1000 micropipette puller and filled with an internal solution containing in mM: 140 $KMeSO_4$, 10 KCl, 10 HEPES, 0.1 EGTA, 2 $MgCl_2$, 4 K-ATP, 0.2 Na-GTP, and 10 phosphocreatine, pH 7.2 at 290-300 mOsm and 5 uM of either Alexa 488 (*ThermoFisher Scientific*). Recordings were amplified and filtered at 10 kHz with an Axon MultiClamp 700B amplifier and digitized at 20 kHz with an integrated general purpose input/output interface (*Bruker, National Instruments*). Experiments and imaging were controlled with PrairieView and a liquid junction potential was measured at −10 mV.

Burst property and excitability experiments

Current clamp experiments were performed with a holding current to maintain resting membrane potential at −70 mV. Recordings were analyzed using custom scripts written in MATLAB (*MathWorks*). For rebound burst characterization, bursting was determined following a 500 ms, −0.5 nA current step. Potential burst events were identified following low-pass filtering at 12 Hz via the 'findpeaks' function implemented in MATLAB (*MathWorks*). Peak events with a prominence greater than two standard deviations of the baseline noise following band-pass filtering were considered bursts.

Basic excitability was assessed with 500 ms square current injections ranging from 10-150 pA. To examine a cell's responsiveness during moderate input, a second protocol in a subset of cells modified this protocol include a fixed 100 pA injection for 600 ms, followed by ten 100 ms steps alternating between 150 and 100 pA.

To systematically examine the changes in spiking rate as a function of input current (S/I curve) for neurons in the auditory thalamus, we fit the S/I curve based on the observed spike rates across current levels for each recorded cell with the Weibull function:

$$W(x) = r_{max} * \left(1 - e^{-\left(x_{/\alpha}\right)^{\beta}}\right)$$

Where *W(x)* was taken as the spiking rate relative to the estimated maximum (r_{max}), and *x* was the injected current. The slope values, α and β, and maximum firing rate (r_{max}) were fitted parameters. An identical fitting procedure was repeated for auditory thalamic neurons in slices taken from KO animals. Similar values were obtained by fitting to a logistic function.

Histology

In Situ *hybridization*

mRNA *in situ* hybridization was performed as described previously (Wells et al., 2016). 20μm cryosections freshly frozen P0, P35 brain sections were hybridized with a mixture of two digoxigenin (DIG)-labeled probes against mouse Ptchd1 cDNA (GenBank Accession NM_001093750.1; ex2 base pairs 372-1006 and ex3 base pairs 1290-2027). The sections were then treated with an alkaline-phosphatase-conjugated anti-DIO antibody (Roche) and labeled with 5-bromo-4-cloroindolyphophate/nitroblue tetrazolium (Roche).

Fluorescence Labeling

To examine fluorescent labeling results, mice were deeply anesthetized and transcardially perfused with phosphate buffered saline (PBS) followed by 4% paraformaldehyde. Brains were dissected, postfixed overnight at 4°C and sectioned in 50μm thickness using a vibratome (LEICA, Buffalo Grove, IL). All sections were imaged on a Zeiss LSM710 confocal microscope (Zeiss, Oberkochen, Germany).

Linear-Nonlinear Poisson Modeling of the effect of audTRN suppression on MGB spiking activity

To better understand and characterize MGB and audTRN neurons as well as to assess how changes in biophysical properties might translate into the observed changes in response properties of these neurons in the KO, we developed a Linear-Nonlinear Poisson (LNP) cascade model of each of these cell types based on standard approaches (Ostojic and Brunel, 2011). More precisely, for excitatory input we approximated the trial averaged firing rate, r(t) of each neuron using the following response function:

$$r(t) = r_{max} * W(F * s(t,f))$$

where $F * s(t,f)$ is the convolution between the linear filter corresponding to the input sensitivity and the signal input and *W* is the nonlinear response filter. The response filter was composed of a vector of channel sensitivities corresponding to different frequencies (240 channel model) while r_{max} is the maximum firing rate of each neuron. A Gaussian sensitivity curve with a full-width at half-maximum of 0.1 octaves (corresponding to the average response width of the main peak for these cells) was used for the response filter. These input channels approximated synaptic input, from inferior colliculus, with weights approximating the sensitivity to different sound frequencies and was based on previous estimates of receptive field characteristics in these neurons (Hackett et al., 2011).

For our simulations, we considered only the weighting function F did not vary with time. The signal input, s_k included an approximation of the sound input as a vector with the same number of frequencies. To generate this vector, each 25 ms "chord" within the

DRC was processed using a previous implementation of erb filter banks to approximate ICS/MGB inputs produced following cochlear filtering as described previously ((Overath et al., 2015), http://mcdermottlab.mit.edu/downloads.html). The input to the non-linear response function for each time point, *F*s(f)* was then given by this input weighted by the neuron's response filter and summed with spontaneous currents:

$$F * s(f) = f_{spont} * I_{spont} + \sum_{k=1}^{n} f_k * s_k$$

Where $f * I_{spont}$ is a spontaneous current multiplied by a weight which is drawn from a Gaussian distribution, f_k is the weighting function for each of the n frequency bands, (indexed by k), and s_k is the power for each frequency band from the erb filtered "chord" sound stimulus.

For the spiking non-linearity, we employed an easily parameterized sigmoidal function (Weibull, (Dhingra and Smith, 2004; Mortensen, 2002; Yang and Chen, 1978)). To parameterize this model, we examined the changes in firing rate for neurons in the auditory thalamus in response to increasing current injections and fit the resulting spike rates for each recorded cell with the Weibull function:

$$W(x) = r_{max} * \left(1 - e^{-\left(\frac{x}{\alpha}\right)^{\beta}}\right)$$

Where *W(x)* was taken as the spiking rate relative to maximum (r_{max}), x the injected current. The slope values, α and β, and maximum firing rate (r_{max}) were the fitted parameters. To adjust this model based on observed firing rates *in vivo*, we used the maximum observed firing rates from each genotype and condition as the saturation rate taken from single unit recordings (r_{max}). We then solved the resulting model for the spontaneous current (I_{spont}) that would produce the observed spontaneous firing rate, allowing us to estimate the relative offset for current inputs across the response function. This estimate was made only for the spontaneous current in recordings from control mice under baseline conditions.

Within this modeling architecture, we considered two potential versions of inhibitory regulation each producing a different effect on responses. In the first model, divisive inhibition was applied uniformly for all frequencies, reducing stimulus-driven currents divisively, corresponding to dendritic inhibition (Miles et al., 1996; Mitchell and Silver, 2003). In the second model, the output nonlinearity itself was divided by inhibitory input to reflect the impact of peri-somatic inhibition (Miles et al., 1996).

QUANTIFICATION AND STATISTICAL ANALYSIS

Behavior

For behavioral studies, preliminary studies provided sufficient information on effect size so that power analyses could be performed to determine the number of mice and sessions needed. The sample number needed was estimated using power analysis in MATLAB (sampsizepwr) with a β of 0.7 (70%). Using this strategy, the required number of animals was determined to be between 3 and 6 mice per cohort across testing conditions, with > / = 4 sessions per animal. For multiple comparisons, non-parametric ANOVA (Kruskal-Wallis H-test, in cases without repeated-measures), repeated-measures 2-way ANOVA (Friedman Test, in cases with repeated-measures) or multiple ANOVA (MANOVA, for cases with multiple orthogonal manipulations and resampling) was performed followed by pairwise post hoc analysis. All post hoc pairwise comparisons used non-parametric rank-sum (unpaired samples) or sign-rank (paired samples) tests.

Spiking Data

As for behavioral data, preliminary studies provided sufficient information on effect size so that power analyses could be performed to determine the number of mice and sessions needed. The sample number needed was estimated using power analysis in MATLAB (sampsizepwr) with a β of 0.7 (70%). For all included electrophysiological experiments, three sessions were recorded from a single mouse and used for power analysis based on the effect size observed in this preliminary cohort. For each statement of statistical difference included in the manuscript, an appropriate statistical comparison was performed. For large sample sets in electrophysiological recordings, the Kolmogorov–Smirnov normality test was first performed on the data to determine whether parametric or non-parametric tests were required. However, in most cases, non-parametric tests were used by default.

Chloride Photometry

For statistical analysis, portions of the fluorescence time-series traces corresponding with different parts of the behavioral were analyzed separately. Prior to analysis of these individual components of the signal, the overall trace was smoothed with a 100 ms Gaussian filter to reduce noise. Our analysis focused on two components extracted from trial signals consisting of: 1. The signal associated with expectation of sound stimuli/noise (anticipation) and 2. The sound evoked component (stimulus). A diagram illustrating distinct response components of an ideal single trial response in the cued noisy discrimination behavior is shown in Figure 3H. The first component, anticipation, was taken as the average area under the curve of the normalized fluorescence signal within each time bin (15 ms bin size) relative to baseline (taken as the average of the 500 ms prior to initiation) over the entire delay period (500 ms following initiation). The second component, associated with the stimulus, corresponded to the area under the curve during the

stimulus period (250 ms window following the start of stimulus presentation). To separate stimulus driven signal from any fluorescence changes due to anticipation, the area was taken relative to the average signal in the latter half of the anticipation period (250 ms prior to stimulus onset).

Once extracted, these signal components were grouped by genotype and condition and used for subsequent analysis. Group comparisons (MANOVA) across components, genotypes, and treatment conditions were made prior to pairwise statistical testing. For all statistical analysis, N values used corresponded to the number of mice.

DATA AND CODE AVAILABILITY

The datasets and custom code supporting the current study have not been deposited in a public repository due to the inclusion of multiple data-types from custom experimental designs. All data and code used is available from the corresponding author on reasonable request.